NASA
Technical
Paper
2996

April 1990

Comparison Between Design and Installed Acoustic Characteristics of NASA Lewis 9- by 15-Foot Low-Speed Wind Tunnel Acoustic Treatment
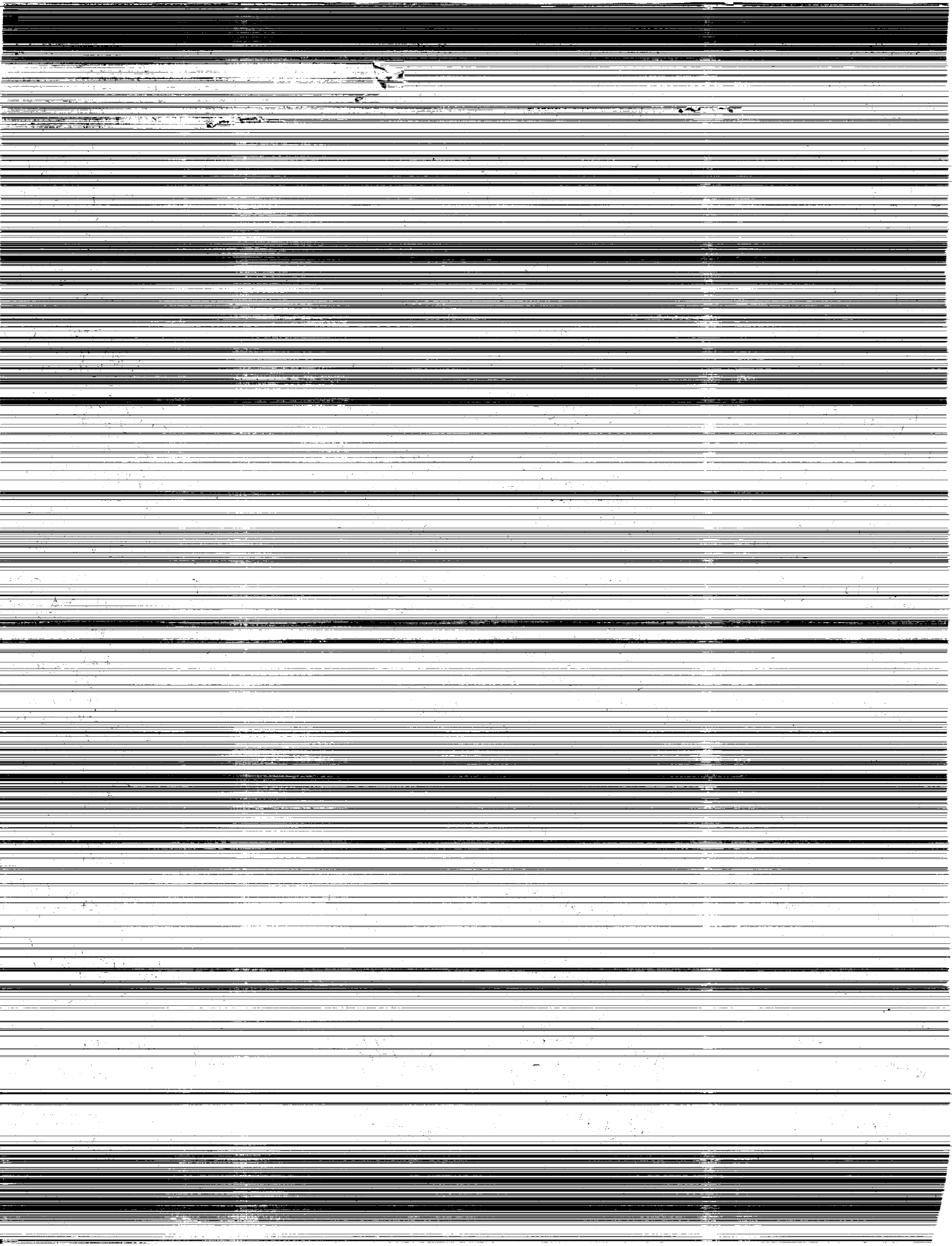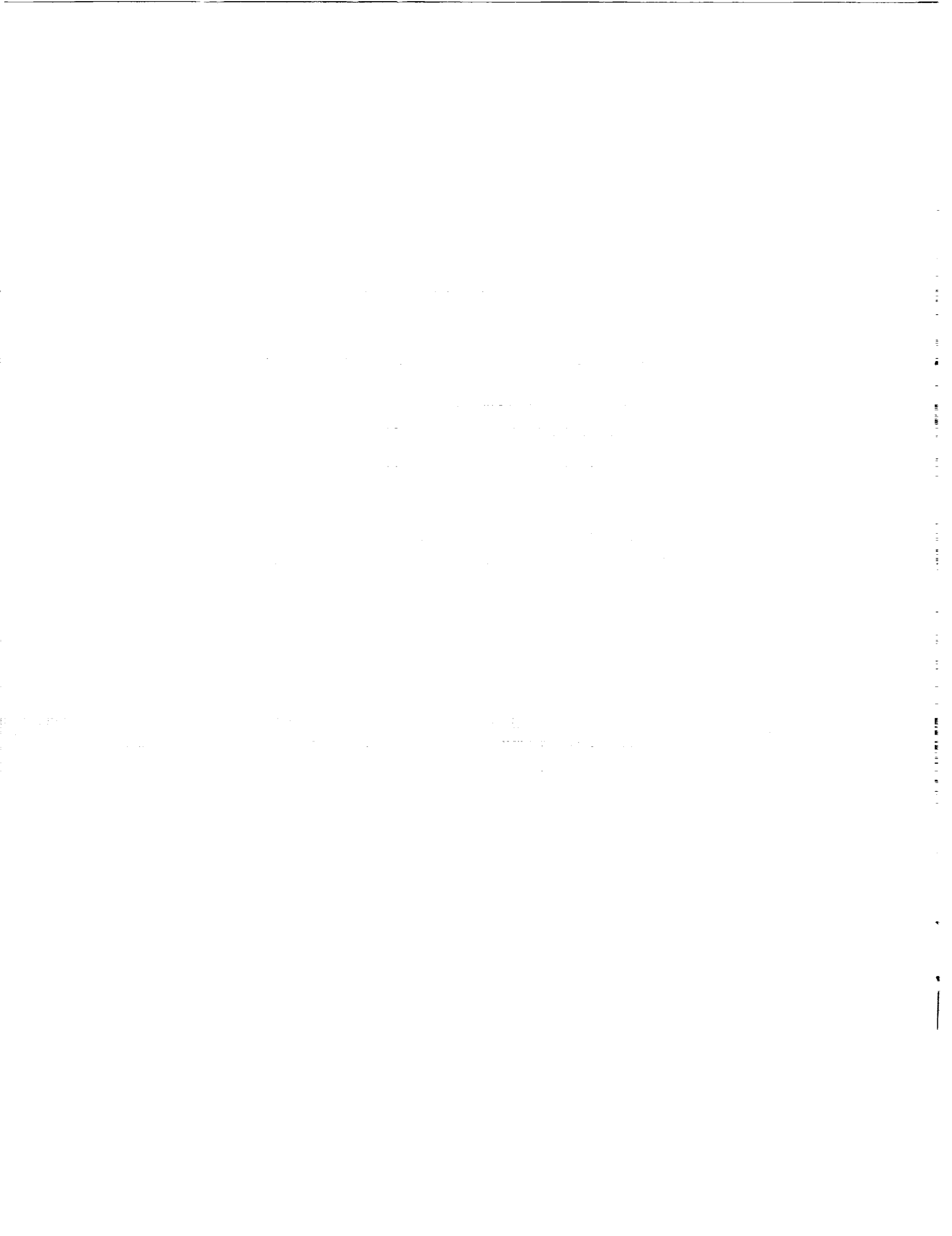
Milo D. Dahl and
Richard P. Woodward

NASA

Comparison Between Design and Installed Acoustic Characteristics of NASA Lewis 9- by 15-Foot Low-Speed Wind Tunnel Acoustic Treatment

Milo D. Dahl and
Richard P. Woodward
Lewis Research Center
Cleveland, Ohio

Summary

The test section of the NASA Lewis 9- by 15-Foot Low-Speed Wind Tunnel was acoustically treated to allow the measurement of sound under simulated free-field conditions. The treatment was designed for high sound absorption at frequencies above 250 Hz and for withstanding the environmental conditions in the test section. In order to achieve the design requirements, a fibrous, bulk-absorber material was packed into removable panel sections. Each section was divided into two equal-depth layers packed with material to different bulk densities. The lower density was next to the facing of the treatment. The facing consisted of a perforated plate and screening material layered together. Sample tests for normal-incidence acoustic absorption were also conducted in an impedance tube to provide data to aid in the treatment design. Tests with no airflow, involving the measurement of the absorptive properties of the treatment installed in the 9- by 15-foot wind tunnel test section, combined the use of time-delay spectrometry with a previously established free-field measurement method. This new application of time-delay spectrometry enabled these free-field measurements to be made in nonanechoic conditions. The results showed that the installed acoustic treatment had absorption coefficients greater than 0.95 over the frequency range 250 Hz to 4 kHz. The measurements in the wind tunnel were in good agreement with both the analytical prediction and the impedance tube test data.

Introduction

The acoustic characteristics of wind tunnel test sections are an important consideration in the measurement of model aircraft propulsion system noise. Under simulated flight conditions, it is desirable to measure the acoustic field directivity to characterize the noise source fully. This is not possible if acoustic reflections from the wind tunnel walls interfere with direct sound from the test model. The solution for reducing interfering reflections has been to line the test section walls with an acoustic material that absorbs the incident sound waves and minimizes the level of any reflections.

The NASA Lewis 9- by 15-Foot Low-Speed Wind Tunnel was designed for determining the performance of aircraft propulsion systems and components at both takeoff and approach conditions. Community noise is an important consideration during takeoff and approach. Measuring the acoustic characteristics of propulsion systems at these conditions was possible after the wind tunnel test section was lined with acoustic material. The 9- by 15-ft test section was originally lined with 3.8-cm-thick fiberglass acoustic material for characterizing the inlet noise from turbofan engines (ref. 1). The lining was designed to reduce acoustic reflections having frequencies above 1000 Hz. When interest was renewed in high-speed turboprop propulsion systems and new general aviation propellers, it became necessary to redesign the acoustic treatment of the 9- by 15-ft test section in order to accommodate the lower frequency noise generated by the propellers. The treatment design goals were to improve the treatment absorption coefficients at low frequencies to 0.97 or higher and to reduce reflections so that measurements could be made in the test section at frequencies of 250 Hz and above. In order to meet this goal, the treatment depth was increased, where possible, from 3.8 cm to 34.4 cm and the fiberglass was replaced with a bulk fibrous material that could withstand the environmental conditions in the test section without breaking down and dispersing into the flow. This design was developed with the aid of both an analytical bulk-absorber treatment model (to predict treatment impedances and absorption coefficients) and low-frequency absorption measurements of treatment samples (ref. 2).

Acoustically treated wind tunnel test sections are commonly calibrated to assess the performance of the installed treatment. The data from such tests typically include measurements of the extent of the acoustic free field for a noise source, the reverberation time, and the levels of the first early reflections from the treated test section walls. Data of this type have been taken in this wind tunnel but are not discussed here. This report describes the impedance and absorption measurements of the installed treatment in order to compare the measured acoustic characteristics of the treatment with the analytical predictions and sample tests on which the treatment design was based. The construction, handling, and installation of the treatment could result in acoustic characteristics that vary from those predicted.

After a description of the test section and the treatment, the choice of the impedance measurement technique is briefly described for normal incidence. This is followed by a discussion of the impedance and absorption coefficient results, and comparisons are made between the analytical predictions for the treatment and the low-frequency impedance tube measurements of the treatment. In the appendixes, a detailed discussion is presented on the measurement technique, which uses the new application of time-delay spectrometry and the

data analysis procedure. In addition, the analytical prediction for a two-layer, bulk-absorber treatment is presented, and the predicted effects of angle of incidence on the treatment characteristics are briefly discussed.

Description of Test Section and Acoustic Treatment

The test section of the 9- by 15-Foot Low-Speed Wind Tunnel is located in the low-speed return leg of the 8- by 6-Foot Supersonic Wind Tunnel (fig. 1(a)). The test section is 2.74 m high by 4.58 m wide by 8.75 m long. The airflow through the test section has a nominal maximum Mach number of 0.2. Four horizontal bleed slots, 10.1 cm wide, extend along each vertical wall for the full length of the test section. Further details on the low-speed wind tunnel may be found in reference 3.

Sectional views of the test section with treatment are shown in figure 1(b). The floor and ceiling are completely treated except where model supports would protrude through the treatment. For the walls, additional treatment is located behind the bleed slots in order to reduce reflections from sound entering the slots from the test section.
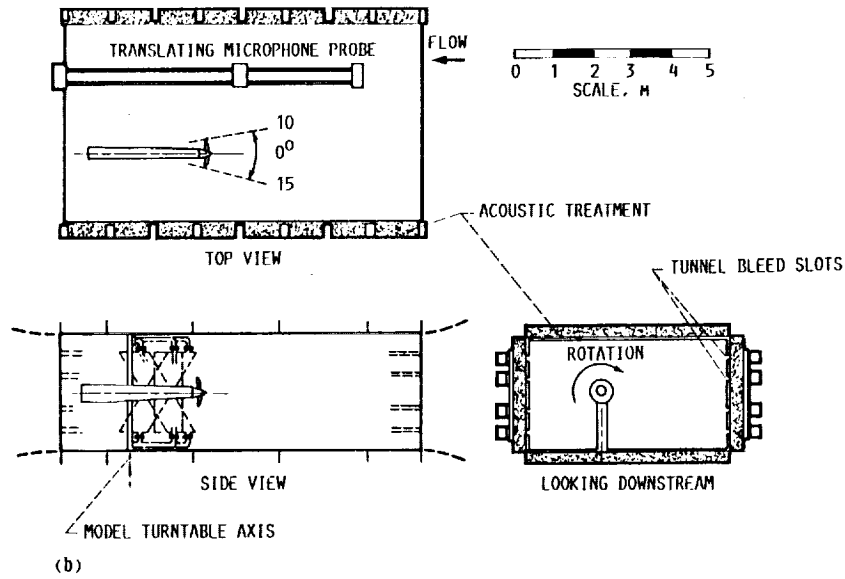
The acoustic treatment consists of boxes with perforated-plate facing to hold the acoustic bulk-absorber material called Kevlar. A typical example is shown in figure 2. The boxes

were designed to fit in among, and be supported by, the structural beams of the wind tunnel. Consequently, the boxes had less than the 34.4-cm depth at those locations where a structural beam was present. For the typical full depth of 34.4 cm, the treatment consisted of two layers of bulk absorber each 17.2 cm thick. As can be seen in figure 2, the structure of the treatment from the front facing to the hard metal backing is as follows: perforated-plate facing, 20-mesh screen (1.3-mm center-to-center wire spacing), first layer of bulk absorber at a nominal bulk density of 6.4 kg/m^3, perforated-plate separator, and a second layer of bulk absorber at a nominal bulk density of 17.7 kg/m^3. The facing and the separator are 40-percent-open perforated plates, 0.16 cm thick. The front perforated plate is backed by a 20-mesh screen as an additional measure to prevent any fibers from the bulk absorber getting into the flow stream. A varnish spray was used to attach the screen to the first sheet of bulk-absorber material. For locations where the structural beams were present, the treatment depth was less than the 17.2-cm thickness of the first layer. The example box in figure 2 shows this thin treatment at both ends of the box. (Further examples are shown in fig. 6.) The bulk-absorber treatment at these locations was packed to the same nominal bulk density, 6.4 kg/m^3, as the first layer of the full-depth treatment. Finally, tube spacers with tie bolts were passed through the treatment (1) to add structural support, (2) to help keep the bulk-absorber material from sagging, and (3) to keep the separator plate in place (see fig. 2).
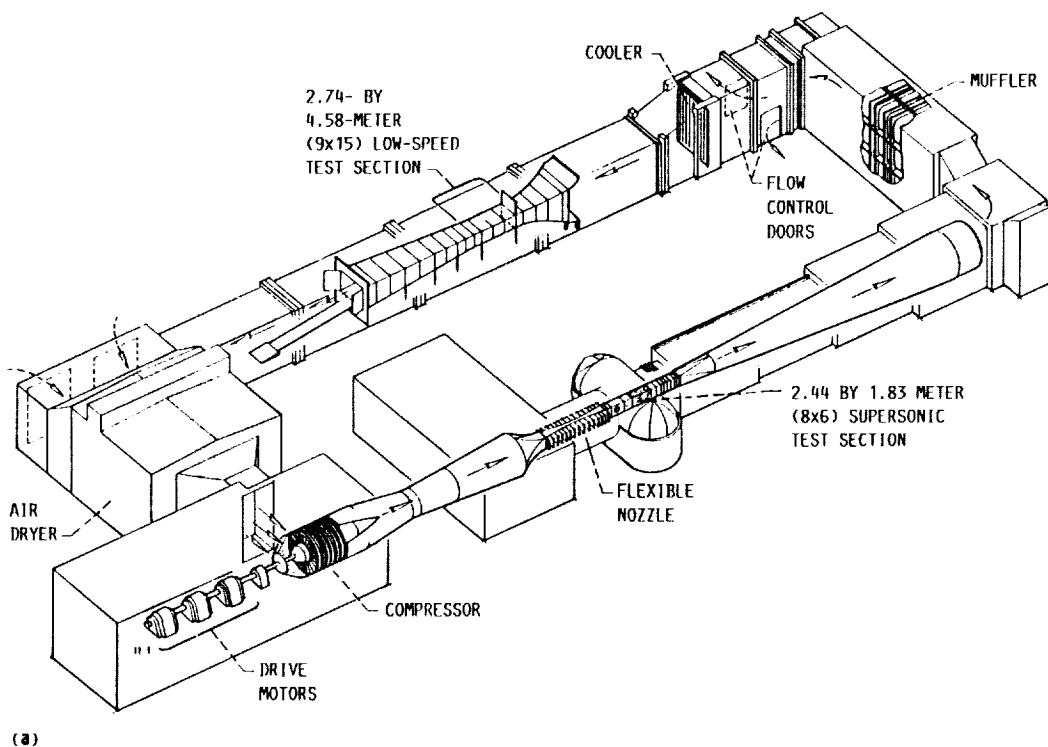
(a) NASA Lewis 9- by 15-Foot and 8- by 6-Foot Wind Tunnels.

Figure 1.—Design of NASA Lewis anechoic wind tunnel.

2

TRANSLATING MICROPHONE PROBE

FLOW

0 1 2 3 4 5
SCALE, M

TOP VIEW

10
0°
15

ACOUSTIC TREATMENT

TUNNEL BLEED SLOTS

ROTATION

SIDE VIEW

LOOKING DOWNSTREAM

MODEL TURNTABLE AXIS

(b)

(b) Sectional views of 9- by 15-Foot Low-Speed Wind Tunnel test section.

Figure 1.—Concluded.

0.16-CM (16 GAUGE)
PERFORATED SEPARATOR PLATE
0.32-CM DIAMETER STAGGERED HOLES
40% OPEN AREA

20-MESH
SCREEN

17.2 CM

17.2 CM

7 KEVLAR SHEETS
(6.4-kg/m^3 EFFECTIVE DENSITY)

18 KEVLAR SHEETS
(17.7-kg/m^3 EFFECTIVE DENSITY)

SIDE VIEW

TOP VIEW

TIE BOLT

PERFORATED SEPARATOR PLATE

TUBES TO SPACE
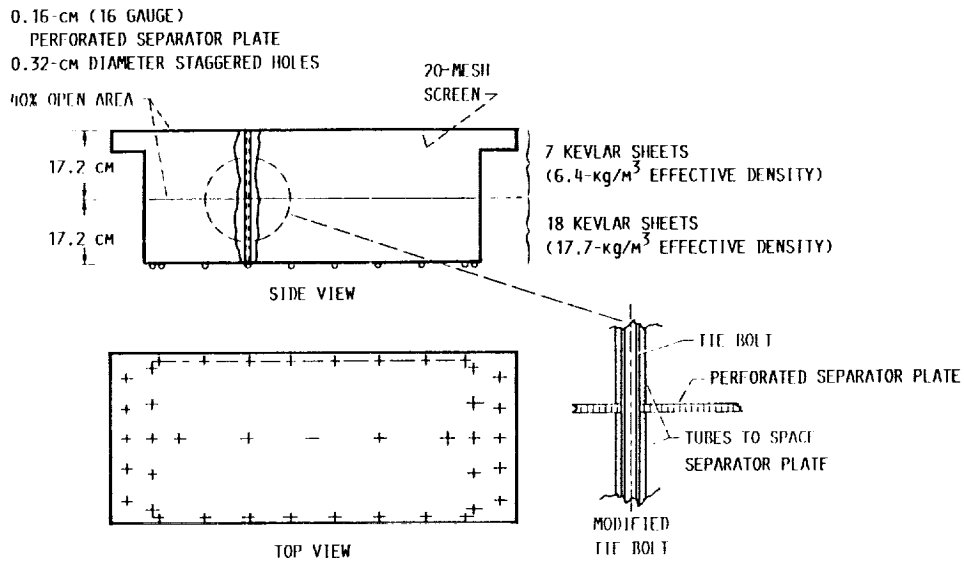SEPARATOR PLATE

MODIFIED
TIE BOLT

Figure 2.—Typical acoustic treatment box for 9- by 15-Foot Wind Tunnel test section. Kevlar: 2.54-cm-thick sheets, 6.4-kg/m^3 density.

Measurement Technique

The acoustic impedance and absorption coefficient measurements of the installed treatment were based on the steady free-field method described by Ingard and Bolt (ref. 4) combined with the use of time-delay spectrometry (TDS) (a measurement technique that uses a swept sine wave to separate signals having different time delays caused by differences in signal path length). This method requires one acoustic source and one microphone placed at the surface to measure the acoustic signal. A measurement is taken with a hard surface that defines, for reference, the amplitude and phase characteristics of the incoming acoustic wave from the source to the surface. The measurement is then repeated with a soft surface and with the identical setup geometry as the hard-surface measurement. By comparing the two measurements, the source characteristics can be eliminated, leaving the data in a form that represents only the effects of a soft surface on an incoming acoustic wave. Ordinarily, the steady free-field method requires that anechoic conditions exist in all directions away from the surface being measured. By combining the method with TDS, however, the necessary anechoic conditions can be simulated by filtering out extraneous reflected signals. Thus, the free-field method can be used with TDS to measure

3

the acoustic properties of the treatment installed in the 9- by 15-ft test section.

This measurement method requires a mathematical model for the sound field that is valid at the surface of the treatment. Instead of using the plane wave analysis of Ingard and Bolt, this report uses the later analysis for incoming spherical waves given by Nobile and Hayek (ref. 5). In general, having measured the pressure p_h at the hard wall and the pressure p_s at the soft wall, p_s is divided by p_h in accordance with the mathematical model

$$\frac{p_s}{p_h} = Me^{i\phi} = \frac{1 + N\left(\dfrac{1 - \beta}{1 + \beta} + Cs\right)}{D} \tag{1}$$

where D is the denominator

$$D = \frac{R_{1s}}{R_{1h}} e^{i\,(k_h R_{1h} - k_s R_{1s})} \left(1 + \frac{e^{ik_h 2\delta_h}}{1 + \dfrac{2\delta_h}{R_{1h}}}\right) \tag{2}$$

N is a numerator factor

$$N = \frac{e^{ik_s 2\delta_s}}{1 + \dfrac{2\delta_s}{R_{1s}}} \tag{3}$$

and Cs is the spherical wave correction factor given in equation (A6). All other quantities are defined in appendix E. The correction factor Cs is a nonlinear function of the specific acoustic admittance β, and therefore, equation (1) must be solved for β by using an iteration technique. Once β is calculated, the specific impedance and the absorption coefficient are determined with the following equations:

$$\frac{z}{\rho_0 c_0} = \frac{1}{\beta} \tag{4}$$

$$\alpha = 1 - \left|\frac{1 - \beta}{1 + \beta}\right|^2 \tag{5}$$

Full details of the mathematical basis of the measurement technique and the data analysis procedure are given in appendixes A and B.

A typical hard-wall measurement setup is shown in figure 3. The face of the horn attached to the acoustic driver was parallel to the hard surface. The distance from the surface to the horn face was measured for each individual setup; in general, this distance was approximately 1.15 m. The figure shows a low-frequency acoustic driver in place with a usable frequency response from 150 Hz to about 7 kHz. In order to obtain data at higher frequencies, this driver was replaced with a high-frequency driver having a usable frequency response from 2 to 10 kHz. The 0.64-cm-diameter condenser microphone was placed against the surface so that the face of the microphone was perpendicular to the surface. For each setup, measurements were again made of the distance from the surface to the center of the microphone. The face of the microphone was located on the axis of the horn.

A typical soft-wall measurement setup is shown in figure 4. This setup repeats the hard-wall setup and measurements were taken of all important dimensions.
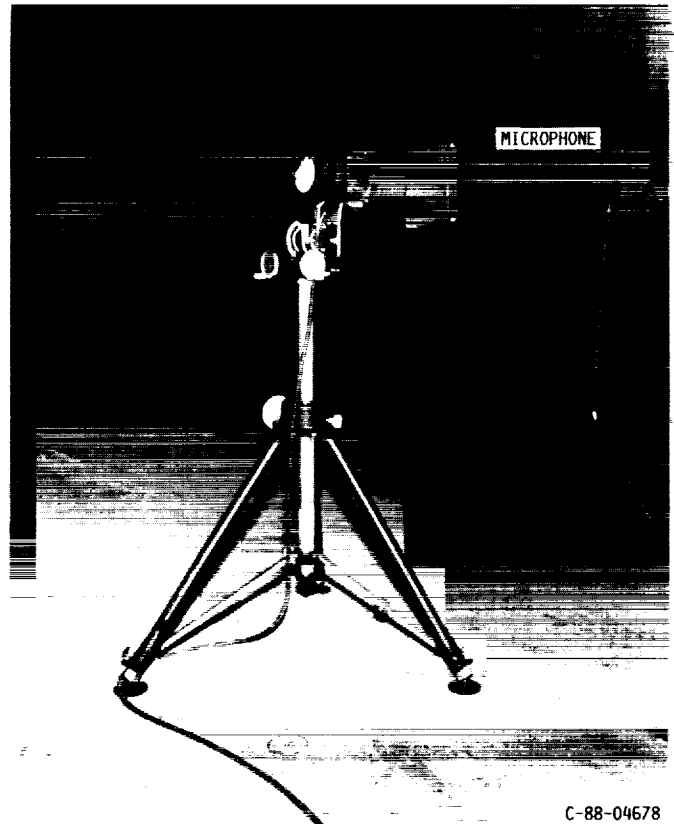

MICROPHONE

C-88-04678

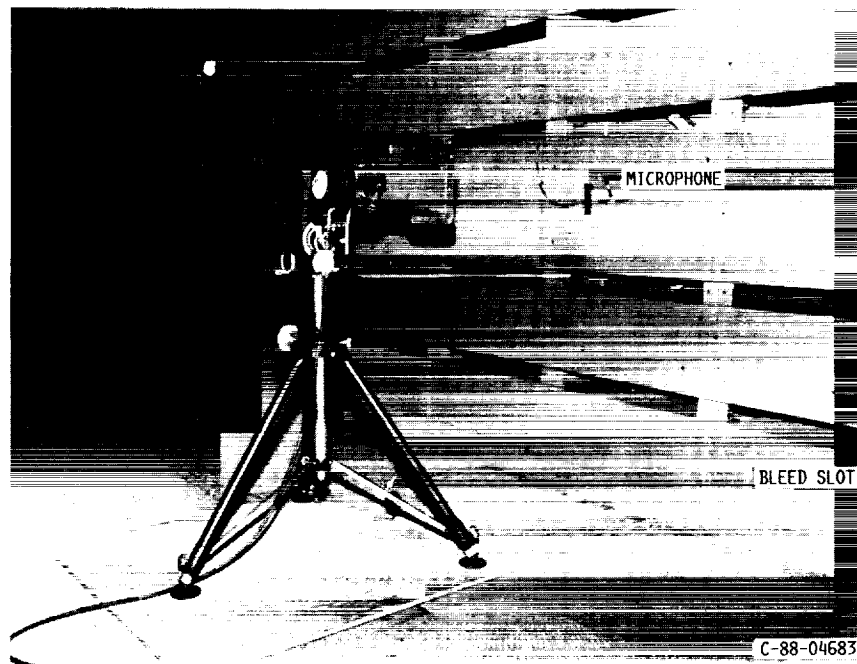Figure 3.—Typical hard-wall setup for normal-incidence measurements.

Figure 4.—Typical soft-wall setup for normal-incidence measurements.

Results and Discussion

The normal-incidence measurement of the acoustic properties of the installed treatment in the 9- by 15-ft test section and the subsequent data analysis were successfully completed for six locations in the test section. These locations on the test section treatment are shown in figure 5, and the spatial positions are given in the accompanying table according to the axis system defined in the figure. The six locations were chosen near the centerline of the ceiling and the wall in order to maximize the path of any unwanted reflection. This enabled the TDS technique to easily filter out the unwanted reflections from the measurement.

Once the hard-wall and the soft-wall measurements were completed, the data analysis procedure described in appendix B was used to determine the admittance of the treatment. Then the impedance and the absorption coefficient were calculated by using equation (B7). The impedance and absorption coefficient results for the six locations are shown in figure 6. For each measurement point, a sketch of the measured treatment box is included to show the relative position of the measurement location viewed from the surface.

A correction was applied to the measured data to account for the uncertainty of both the starting point of acoustic radiation and any electromechanical delay within the acoustic driver. The correction represents a small unknown time delay within the system. The details of the correction procedure, which only applies for highly absorptive materials, are given in appendix B. The error corrections used in calculating the results shown in figure 6 are given in table I. Measurement points 1, 2, 4, and 6 include both low- and high-frequency corrections because data were taken with two acoustic sources having different frequency ranges, as discussed in the previous section. In correcting the data for points 1, 2, and 4, the low frequencies were handled in the manner described in appendix B. Because absorption in the treatment apparently decreased at the higher frequencies, a correction factor for the high-frequency data could only be determined by using the data in the 2- to 4-kHz region. This region had high absorption (as required for the correction procedure), and it overlapped the 2- to 4-kHz region of the low-frequency data. Thus, the high-frequency data correction factor was adjusted as necessary to ensure that the admittance calculated from the high-frequency data matched the admittance calculated from the low-frequency data with a minimum of error in the overlap region from 2 to 4 kHz. Because of the poor absorption at lower frequencies, point 6 was corrected in the opposite manner, with the high-frequency range corrected first and the low-frequency range corrected with the matching criterion. No high-frequency data were taken at points 3 and 5. In all cases shown in table I, the error corrections were well within the time resolution for the TDS measurements of ± 62.5 μs, indicating that a small time delay within the measurement system could not be accurately resolved during the measurement.

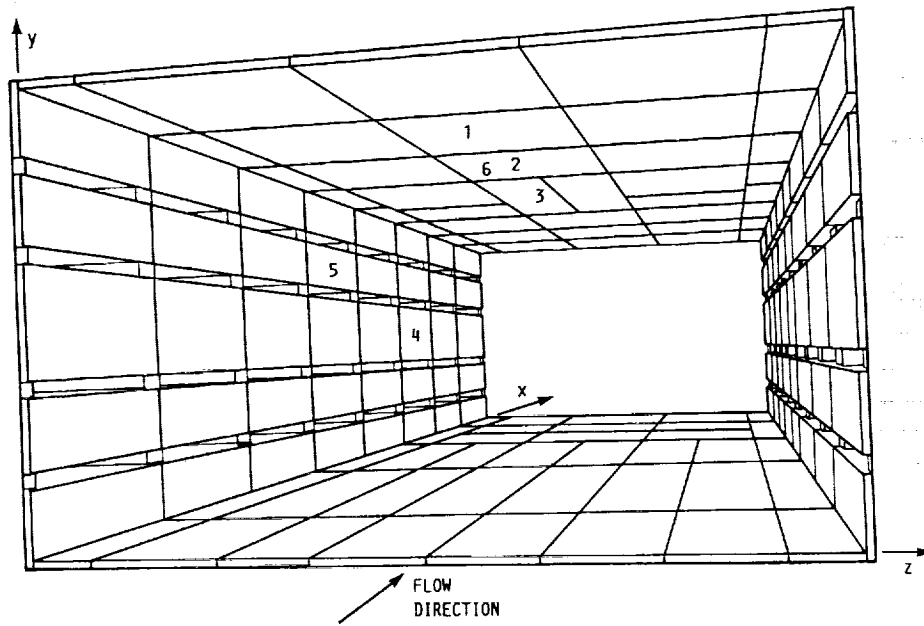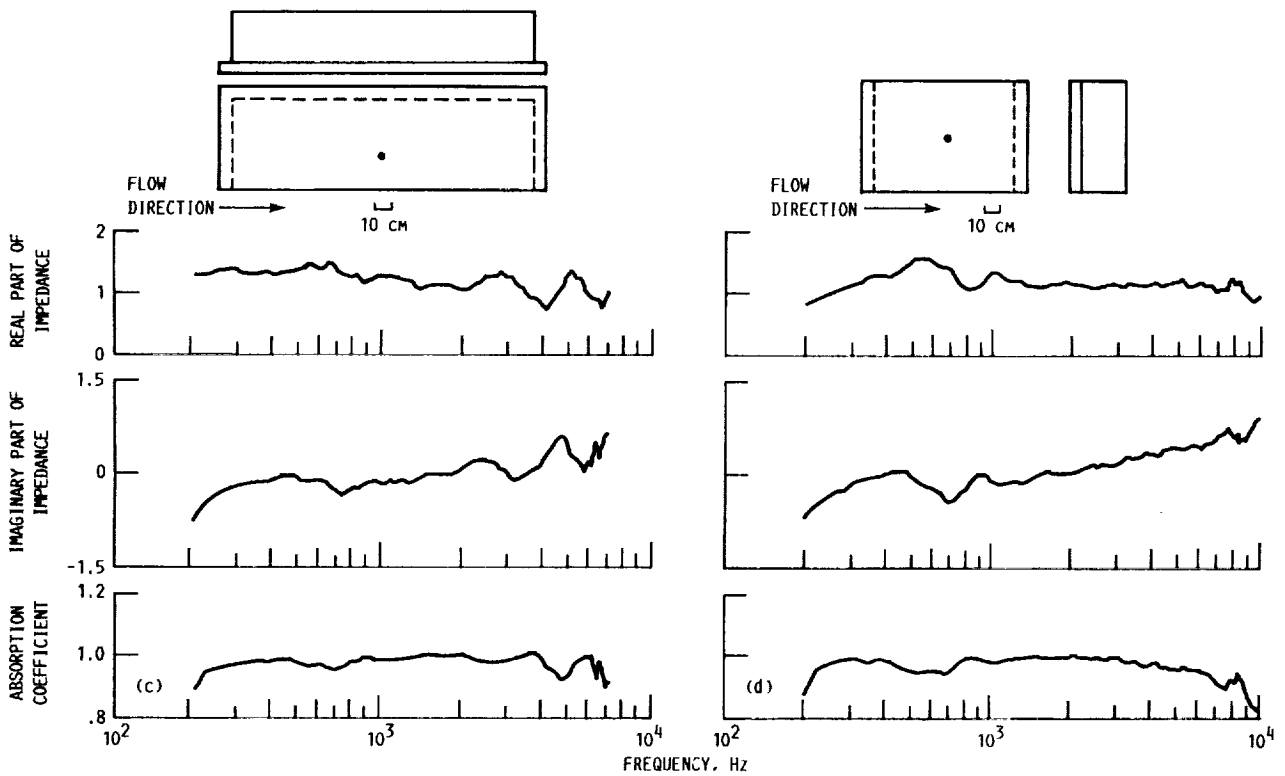| MEASUREMENT POINT	LOCATION OF MEASUREMENT POINTS AROUND X, Y, AND Z AXES, M		
	X AXIS	Y AXIS	Z AXIS
1	1.73	2.74	2.09
2	2.74	2.74	2.11
3	4.26	2.74	2.12
4	5.59	1.33	0
5	3.76	1.95	0
6	3.07	2.74	1.79

Figure 5.—Perspective view of 9- by 15-foot treated test section showing location of impedance measurement points.
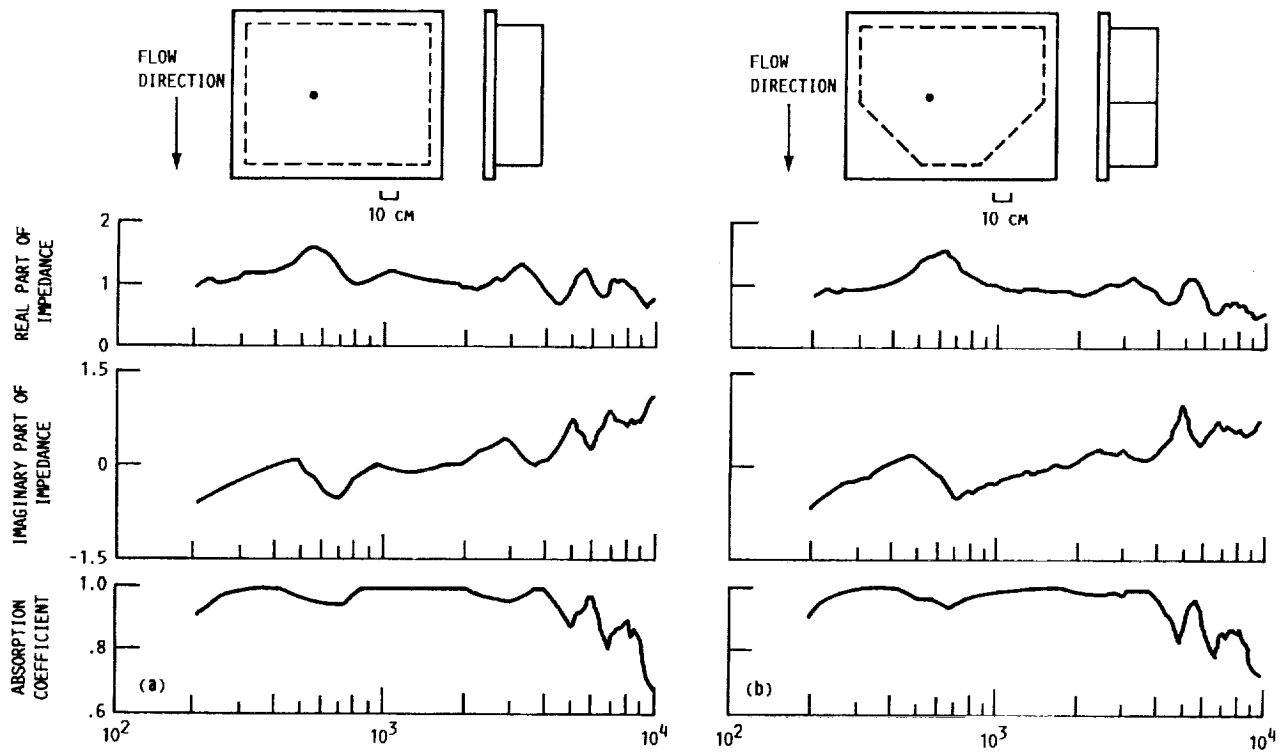
(a) Measurement point 1.
(c) Measurement point 3.

(b) Measurement point 2.
(d) Measurement point 4.

Figure 6.—Calculated impedance and absorption coefficient from normal-incidence measurements of installed treatment in 9- by 15-foot test section. Location of measurement point on acoustic treatment box shown in sketch of each box.
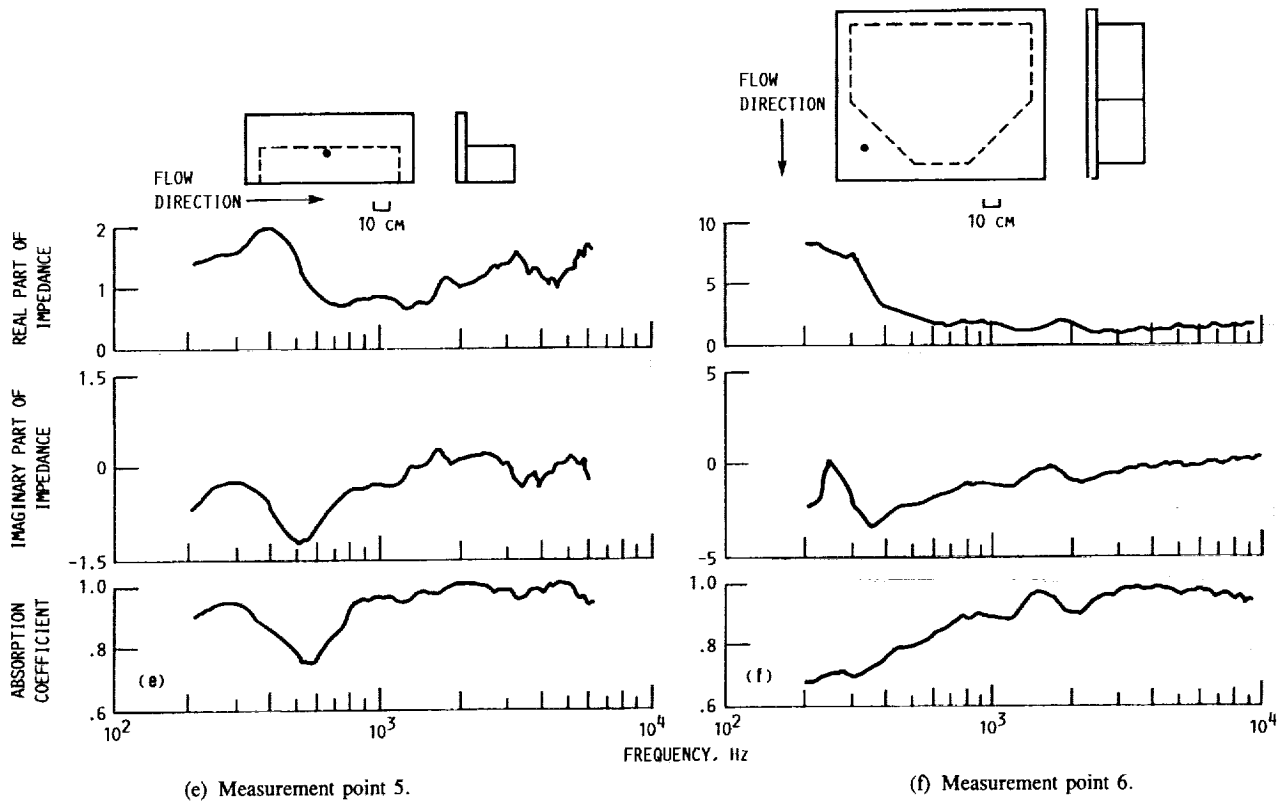
(e) Measurement point 5.

(f) Measurement point 6.

Figure 6.—Concluded.

TABLE I.—CORRECTIONS APPLIED TO NORMAL-
INCIDENCE MEASUREMENTS

[Calculated from equation (B12) for impedances shown in figure 6.]

Measurement point	Low frequency		High frequency	
	Impedance, Z, μs	Frequency, f, kHz	Impedance, Z, μs	Frequency, f, kHz
1	14.12	<5.4	−5.63	>5.4
2	2.69	<5.0	−5.16	>5.0
3	9.66	<7.0	———	——
4	2.46	<3.0	−7.89	>3.0
5	16.25	<6.0	———	——
6	20.36	<3.0	−.64	>3.0

Measurement points 1 to 4 were all full-depth treatment regions. A comparison of figures 6(a) to (d) shows that the impedances and the absorption coefficients were similar at these locations. The major difference was that the wall location (point 4, fig. 6(d)) lacked the large oscillations at the higher frequencies. As an indication of the impedance and absorption coefficients for the full-depth installed treatment, the results from these four locations were averaged together. Figure 7 shows the averaged values and one standard deviation from
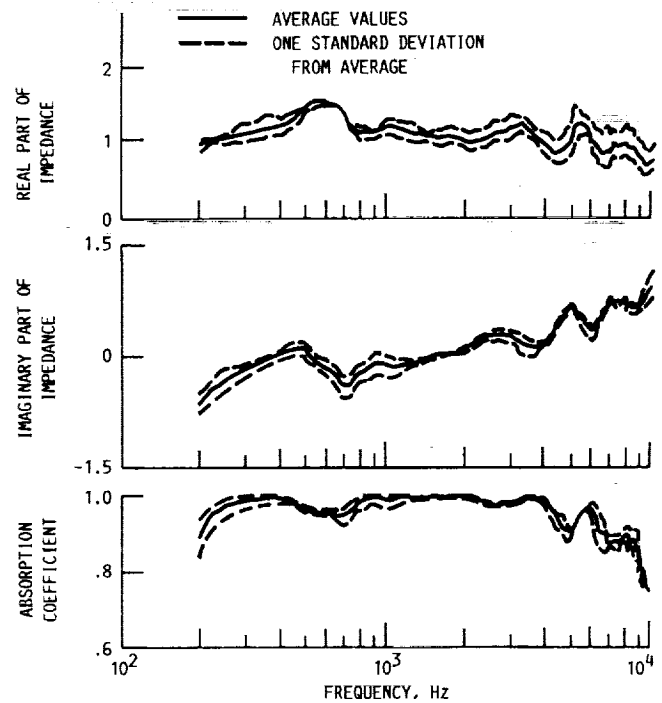

Figure 7.—Averaged impedance and absorption coefficient results for full-depth installed treatment in 9- by 15-foot test section.

the average for this limited amount of data. These results show that the treatment had high normal absorption near 1 from about 250 Hz to 4 kHz, with a slight dip in absorption down to 0.95 in the 500- to 700-Hz region. The largest deviation from the average absorption coefficient was 0.03. This is a good indication that the high absorption for the full-depth treatment was maintained over the 250-Hz to 4-kHz frequency range for the treatment in the test section. At frequencies greater than 4 kHz, the absorption began to decrease.

Figure 8 compares the averaged results at frequencies less than 2 kHz with both low-frequency impedance tube measurements of a treatment sample and analytical predictions for the treatment. The impedance tube measurements were conducted as described in reference 2 with a sample constructed in a manner identical to that shown in figure 2 for the full-depth treatment. The sample absorption coefficient curve does not oscillate much at frequencies above the low-frequency rolloff point. This compares well with the analytical predictions for a two-layer treatment using model 1 to describe the acoustic characteristics of the material packed in each layer of the treatment (see appendix C). On the basis of the sample tests and the absorption characteristics predicted for the treatment using model 1, the treatment design goal of an absorption coefficient of 0.97 or higher at frequencies above 250 Hz was considered to be achieved.

By contrast, the averaged installed treatment absorption coefficient curve has a larger oscillation than the sample curve. Its characteristics tend to be similar to an analytical prediction for a two-layer treatment using model 2 rather than to a prediction using model 1. In the final comparison between the prediction using model 1, the sample absorption coefficients, and the average installed treatment absorption coefficient, the difference was small. The lowest installed treatment absorption coefficient of 0.95 near 700 Hz indicated only a 2-dB increase in reflected energy above that which would have been achieved with the design goal of 0.97 for the absorption coefficient.

Over the full measured frequency range, figure 9 compares the prediction for the two-layer treatment using material
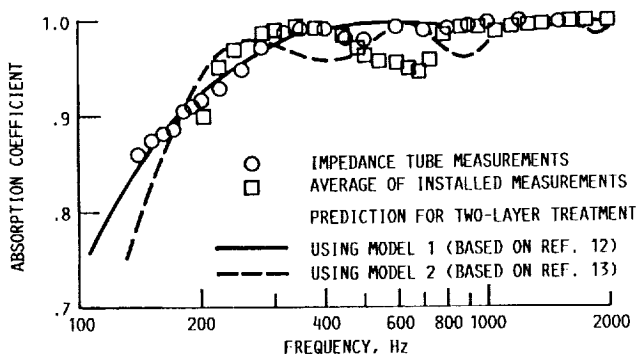

Figure 8.—Absorption coefficient comparison between sample impedance tube measurements, average installed treatment measurements, and two treatment models.
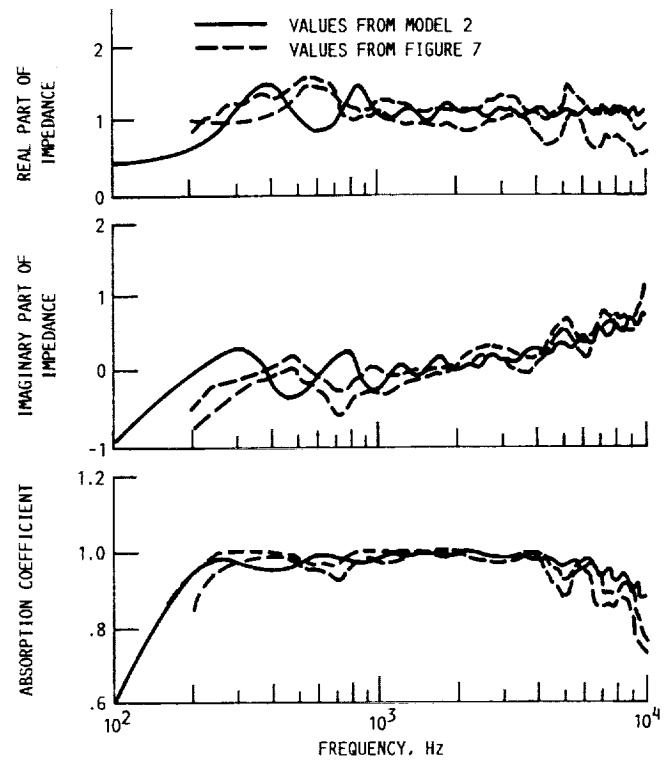

Figure 9.—Impedance and absorption coefficient comparisons between predictions for two-layer treatment using model 2 and range of measured installed treatment values from figure 7.

model 2 with the range of measured impedance and absorption coefficient values (based on ± 1 standard deviation from the average values as shown in fig. 7) for the installed treatment. In addition to the low-frequency similarities, the analytical predictions show the decrease in absorption at high frequencies. The reactance of the treatment impedance moves away from zero significantly as the frequency increases. This is due primarily to the presence of the perforate at the face of the treatment. To improve high-frequency absorption, the perforated plate would have to be replaced or covered over by a thin layer of absorbing material. However, if the resistance of the new facing is higher at the low frequencies than that of the perforated plate, the improved higher-frequency absorption will be gained at the expense of a loss in low-frequency absorption.

Concluding Remarks

The acoustic impedances and the absorption coefficients were determined for the installed acoustic treatment in the test section of the NASA Lewis 9- by 15-Foot Low-Speed Wind Tunnel from normal-incidence measurements. These measurements were conducted in order to compare the installed treatment with analytical predictions and sample tests on which the treatment design was based.

9

The treatment was measured with a new application of time-delay spectrometry combined with an established free-field method. This allowed the acoustic signal to be measured near the face of the treatment and eliminated the effects of other reflected signals in the test section. The treatment could thus be measured when installed in the test section.

After data analysis, the impedances and the absorption coefficients were presented for six measurement points in the test section. Four of these measurement points were full-depth treatment locations, and the results were similar for all four points. Thus, the full-depth results were combined in order to obtain an average normal-incidence impedance and an average absorption coefficient for the test section treatment. The full-depth installed acoustic treatment had an absorption greater than 0.95 from 250 Hz to 4 kHz. At frequencies above and below this range, the absorption steadily decreased. This was in agreement with the analytical predictions and the sample impedance tube tests at the lower frequencies, where sample test data were available. At the higher frequencies, the installed treatment impedances and absorption coefficients could only

be compared with the analytical predictions, and the results from normal-incidence measurements were found to be in good agreement with the predictions. Furthermore, even though no angle-of-incidence measurements have been properly made for the treatment in the 9- by 15-ft test section, predictions in appendix D show that the absorption coefficient does not change significantly out to a 45° angle of incidence from normal. This 45° angle is about the maximum angle of incidence that an acoustic signal would make with any treated surface in the test section for typical source and microphone positions used during wind tunnel testing. The normal incidence measurements are therefore good indicators of the treatment's impedances and absorption coefficients.

Lewis Research Center
National Aeronautics and Space Administration
Cleveland, Ohio, October 4, 1989

Appendix A
Measurement Techniques

Many techniques for measuring the acoustic characteristics of large samples of sound-absorbing treatment have been devised. The most common techniques require that an acoustic source be placed away from the treatment, with one or more microphones being used to measure the sound field created by the source in the presence of the treatment.

One of these techniques is based on the ability to separate incident and reflected waves from a soft wall by using unsteady signals such as impulses, tone bursts, or swept sine waves. The time domain signal recorded during the measurement is then filtered in order to extract the desired incident and reflected signals and to suppress any other unwanted reflected signals or noise. The absorption coefficients of the treatment are easily measured by using this method.

Other techniques are based upon the measurement of the steady sound field in front of the treatment. This requires that no interfering reflections affect the measurement. In order to meet this requirement, a large sample must be placed in an anechoic chamber. A mathematical model for the sound field in the presence of an absorbing boundary is developed and the desired absorption and impedance for the treatment are obtained from the data by using that model.

In this study, the acoustic impedance and absorption coefficient measurements of the installed treatment were based on the steady, free-field method described by Ingard and Bolt (ref. 4) combined with the use of time-delay spectrometry (a swept sine wave technique). This method requires one acoustic source and one microphone placed at the surface to measure the acoustic signal. A measurement is taken with a hard surface that defines, for reference, the amplitude and phase characteristics of the incoming acoustic wave from the source to the surface. The measurement is repeated with a soft surface by using the identical setup geometry as the hard-surface measurement. By comparing the two measurements, the source characteristics can be eliminated. This leaves the data in a form that represents only the effects of a soft surface on an incoming acoustic wave. Ordinarily, the steady, free-field method requires that anechoic conditions exist in all directions away from the surface being measured. However, by combining the method with time-delay spectrometry, the necessary anechoic conditions can be simulated by filtering out extraneous reflected signals. The free-field method can thus be used with time-delay spectrometry to measure the acoustic properties of the treatment installed in the 9- by 15-ft test section.

A typical hard-wall measurement setup is shown in figure 3. The face of the horn that was attached to the acoustic driver was parallel to the hard surface. The distance from the surface to the horn face was measured for each individual setup; in general, this distance was approximately 1.15 m. Figure 3 shows a low-frequency acoustic driver in place with a usable frequency response from 150 Hz to about 7 kHz. In order to obtain data at higher frequencies, this driver was replaced by a high-frequency driver with a usable frequency response from 2 to 10 kHz. The 0.64-cm-diameter condenser microphone was placed against the surface such that the face of the microphone was perpendicular to the surface. The face of the microphone was located on the axis of the horn. For each setup, measurements were again made of the distance from the surface to the center of the microphone.

A typical soft-wall measurement setup is shown in figure 4. The setup repeats the hard-wall setup and measurements were taken of all important dimensions.

Equations Governing the Free-Field Measurement Method

The free-field measurement method requires a mathematical model for the sound field that is valid at the surface. Instead of using the plane wave analysis of Ingard and Bolt, this report uses the later analysis for incoming spherical waves given by Nobile and Hayek (ref. 5). The sound field for the hard-wall measurement is governed by an equation (eq. (20) from ref. 5 with $\beta = 0$ for a hard wall, with pressure being used instead of velocity potential)

$$p_h = -i\omega\rho_0 A \left(\frac{e^{ik_h R_{1h}}}{R_{1h}} + \frac{e^{ik_h R_{2h}}}{R_{2h}} \right) \qquad (A1)$$

where R_{1h} is the distance from the source to the microphone and R_{2h} is the distance from the image source to the microphone. The parameter A describes the amplitude and directivity characteristics of the source. For normal-incidence measurements

$$R_{2h} = R_{1h} + 2\delta_h \qquad (A2)$$

where δ_h is the distance from the wall to the microphone. Thus, equation (A1) becomes

$$p_h = -i\omega\rho_0 A \frac{e^{ik_h R_{1h}}}{R_{1h}} \left(1 + \frac{e^{ik_h 2\delta_h}}{1 + \dfrac{2\delta_h}{R_{1h}}} \right) \qquad (A3)$$

In general, the equations for the sound field in front of a soft wall depend upon whether the treatment is considered to be one of local reaction or one of extended reaction (see discussion in ref. 6, section 6.3). For normal-incidence measurements, however, both types react in a similar manner.

Therefore, the local reaction model of Nobile and Hayek is used to describe the sound field in front of the treatment. The general equation (eq. (35b), ref. 5) is

$$p_s = -i\omega\rho_0 A \left\{ \frac{e^{ik_sR_{1s}}}{R_{1s}} + \frac{e^{ik_sR_{2s}}}{R_{2s}} \right.$$

$$\left. - 2ik_s\beta e^{-ik_sR_{2s}\beta} \; Ei\left[ik_sR_{2s}\,(1+\beta)\right] \right\} \qquad (A4)$$

where Ei is the exponential integral and β is the normalized admittance of the locally reacting surface. (The admittance is the inverse of the impedance.) For $k_sR_{2s} > 3$, a valid condition for our measurements, we used the asymptotic expansion for Ei to get

$$p_s = -i\omega\rho_0 A \left[\frac{e^{ik_sR_{1s}}}{R_{1s}} + \frac{e^{ik_sR_{2s}}}{R_{2s}} \left(\frac{1-\beta}{1+\beta} + Cs\right) \right] \qquad (A5)$$
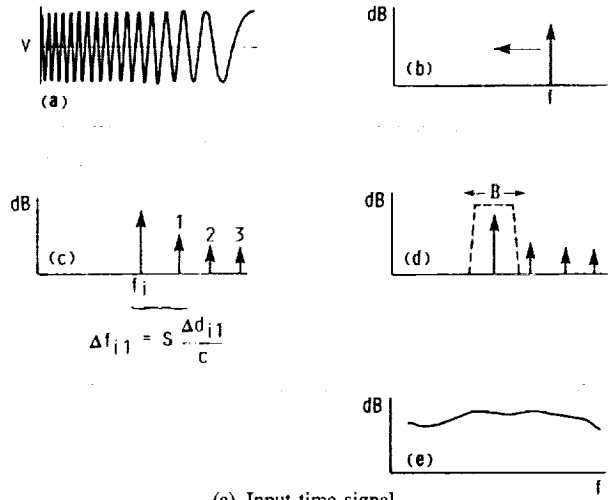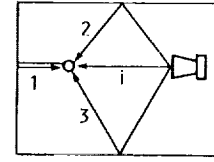
where

$$Cs = \frac{2\beta}{1+\beta} \left\{ \frac{1}{\left[-ik_sR_{2s}(1+\beta)\right]} \right.$$

$$\left. - \frac{2}{\left[-ik_sR_{2s}(1+\beta)\right]^2} + \ldots \right\} \qquad (A6)$$

With the soft-wall image source distance R_{2s} having the same form as equation (A2), equation (A5) becomes

$$p_s = -i\omega\rho_0 A \; \frac{e^{ik_sR_{1s}}}{R_{1s}} \left[1 + \frac{e^{ik_s2\delta_s}}{1 + \frac{2\delta_s}{R_{1s}}} \left(\frac{1-\beta}{1+\beta} + Cs\right) \right]$$

$$\qquad (A7)$$

Use of Time-Delay Spectrometry With Free-Field Method

The fundamental concepts of time-delay spectrometry (TDS) are shown in figure 10. TDS, which is based on the work of Heyser (ref. 7), uses a linear, swept-frequency sine wave to excite the system under test. The source signal is illustrated in figure 10(a) for a sweep from a higher frequency to a lower frequency. Figure 10(b) shows the idealized instantaneous frequency plot for this time signal. It represents a single frequency spike moving with time across the frequency spectrum at a constant sweep rate S (hertz per second). When the sweep signal is applied to the system with the geometry

(a) Input time signal.
(b) Instantaneous frequency.
(c) Receiver signal, where S is sweep rate in hertz per second and time delay is converted to frequency shift.
(d) Tracking filter applied.
(e) Filter output. Resolution, $\Delta f = 1/T = S/B$.

Figure 10.—Fundamental concepts of time-delay spectrometry.

schematically shown in the figure, it travels simultaneously through each of the paths to the receiver. Because each of the paths is of a different length, the signals arrive at different times, assuming a constant propagation velocity c. If the incident path i is used as a reference, each reflected path signal arrives at a time $\Delta d_{ij}/c$ later than the incident signal, where Δd_{ij} is the path length difference between the incident path i and the particular reflected path j. In essence, TDS converts these time delays into frequency shifts as shown in figure 10(c) for the receiver signal. For instance, by the time the first reflected signal arrives, the incident signal has shifted by an amount $\Delta f_{il} = S \Delta d_{il}/c$. The consequence of this frequency shift is the ability to apply a tracking filter that moves with the desired signal at the same sweep rate. The bandwidth B of the tracking filter must be narrow enough so that the effects of all the other signals are eliminated. Figure 10(d) shows an example in which a tracking filter (represented by dashed lines) is applied to the incident signal and all the reflected signals are suppressed. For this case, the output of the tracking filter is the frequency response (magnitude and phase) of the source with frequency resolution $\Delta f = S/B$ (fig. 10(e)).

There are many cases in which TDS could be used to separate the incident and first reflected signals in order to get data for characterizing an acoustically absorbent surface. However, two factors made this approach of measuring the

acoustic treatment difficult to apply in the 9- by 15-ft test section. First, the geometry of the test section made signal path time differences small and, second, the highly absorbent walls of the test section made reflected signals much smaller than the incident signal. The resulting instantaneous receiver signal for a measurement that was to separate incident and first reflected signals in the 9- by 15-ft test section is illustrated in figure 11(a). The incident signal i and the first reflected signal 1 are close together because of a small path time difference; in addition, the incident signal is much larger than the first reflected signal because of high-wall absorption. The illustrated tracking filter is attempting to measure only the first reflected signal; as shown, however, the incident signal would still be large enough to interfere significantly with the measurement of the reflected signal. Consequently, the tracking filter would need to have a narrow bandwidth if it is to keep a large incident signal from influencing the output of the filter that is tracking the first reflected signal. On the basis of the equation $\Delta f = S/B$, this would result in an unacceptably large frequency resolution. Theoretically, the sweep rate S could be reduced as the bandwidth is reduced in order to keep Δf constant. In practice, however, this use of TDS to measure a low-level reflected signal with a narrow bandwidth filter, with slow sweeps, and with long measurement times, did not produce satisfactory results.

These difficulties in using TDS to separate incident and first reflected signals were overcome by combining the TDS

(a) Microphone away from surface.
(b) Microphone at surface.

Figure 11.—Effect of placing microphone at treatment surface on instantaneous receiver signal and tracking filter bandwidth, B. Incident signal, i; first reflected signal, 1; second reflected signal, 2; third reflected signal, 3.

technique with the free-field measurement method. As described previously, the free-field method requires that the microphone be placed at the surface of the treatment. This resulted in changing the instantaneous receiver signal from the pattern illustrated in figure 11(a) (for a microphone away from the treatment surface) to the signal pattern illustrated in figure 11(b) (for a microphone at the treatment surface). The first reflected signal has moved to the position where it arrives at the receiver at almost the same time as the incident signal. By using TDS, the incident and first reflected signals are combined within the bandwidth of the tracking filter (represented by the dashed lines), and later-arriving signals are removed from the measurement to simulate the anechoic conditions required for the free-field method. Because the filter bandwidth can be much larger for the case shown in figure 11(b), better frequency resolution was obtained than for the case shown in figure 11(a).

There was concern in the use of TDS measurements as to how the treatment would respond to a sweeping signal. It was conceivable that the reflected signal would not interact properly with the incident signal because of the transient nature of the signal. The free-field method assumes that a steady-state sound field exists in order to properly measure p_h and p_s as they were derived in equations (A3) and (A7). Two calculation methods were used for estimating a time for the reflection to return from the treatment. One method was to consider the time it took for the signal to travel through the treatment and back out again. An analytical prediction for the treatment (based on material model 2 described in appendix C) was used to calculate the phase speeds in the treatment. The total time it took for an acoustic signal to travel through the treatment, reflect off the back wall, and return to the surface was found to depend on the signal frequency. The times for the reflections to return to the surface were found to steadily decrease with higher frequencies. Therefore, when 200 Hz was chosen as the lowest frequency of interest, the longest reflection time was 2.9 ms. At all higher frequencies, the reflection time was shorter. A second method was to estimate the time it took the treatment to react to an incident wave before the incident wave was reflected. If we assume the incident signal to be a succession of simple harmonic waves each with its own time delay upon intersecting the surface, we can calculate a group delay time (ref. 8)

$$t' = \frac{\partial \psi}{\partial \omega} \tag{A8}$$

where ψ is the phase of the reflection coefficient calculated from equation (C3) for material model 2. Except for frequencies associated with the treatment depth, t' was less than 4 ms for frequencies greater than 200 Hz. This later time t' is a better indicator of the reflection time than the reflection time caused by phase speeds because it applies to a small band of frequencies that react similarly to the treatment. For TDS
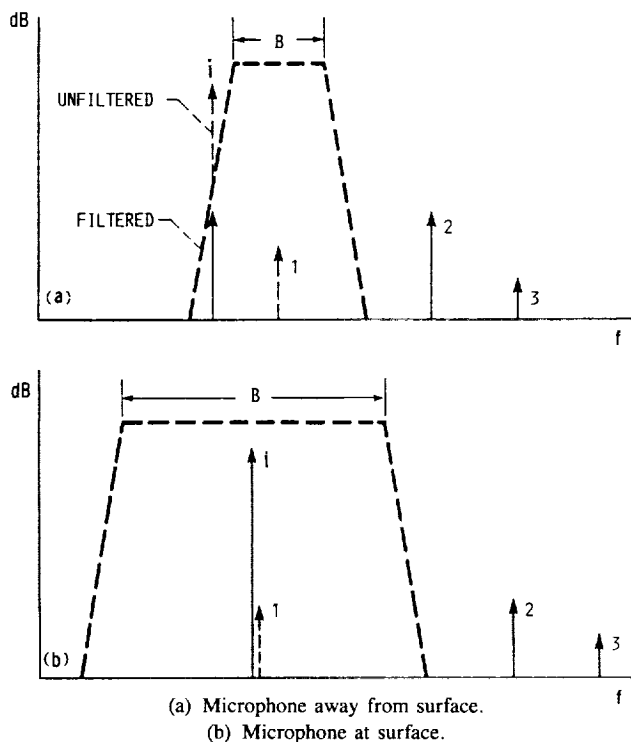
measurements, the time that a signal dwells in the tracking filter is $T = B/S$. This leads to the choice of the sweep rate S and the filter bandwidth B such that $T \geq t'$ to ensure that the reflected signal is interacting with the incident signal, with the additional constraint that T is small enough so that undesirable signals are rejected from the measurement. If $T = 4$ ms is chosen as the worst-case reflection time, $B = 4$ Hz and $S = 1000$ Hz/s are appropriate for proper measurement of the desired signal, which consists of the combined incident and reflected signals at the treatment surface and the suppression of unwanted signals. Thus, for a band of frequencies of width B having the same effect on the treatment, the measurement may be considered to be quasi-steady within the time that any frequency is measured.

Finally, in order to calculate impedance by using equation (A3) for p_h and equation (A7) for p_s, the two separate

measurements must have source signals with the same starting phase. This was accomplished with a digitally based TDS measurement system that generated the sweeping source signal with a consistent starting phase. In order to verify the procedure, a test of the TDS system was conducted in an impedance tube with an arbitrary test sample. As a basis for comparison, the same sample was measured with the two-microphone technique. The results are shown in figure 12. The two techniques gave basically the same results for both the absorption coefficient and the impedance. This indicates that the phase between the hard-wall and soft-wall TDS measurements was properly controlled. The frequency resolution of the TDS measurement was much larger than that of the two-microphone measurement, and therefore the variations measured at the lower frequencies with finer resolution did not show up in the TDS measurement.
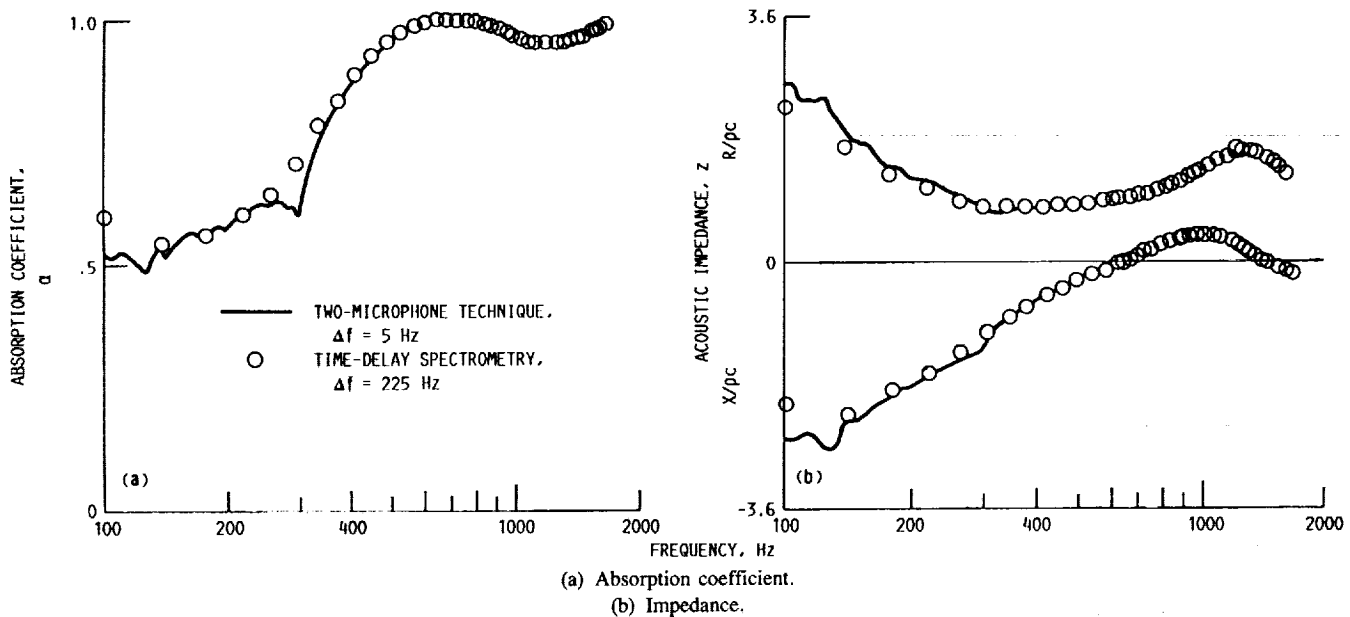

(a) Absorption coefficient.

(b) Impedance.

Figure 12.—Comparison between two-microphone technique and time-delay spectrometry technique. Impedance measurements taken in rectangular duct with plane acoustic waves.

Appendix B
Data Analysis

The data for each soft-wall measurement point consisted of two spectra, each with magnitude and phase: one spectrum for the soft-wall case and one spectrum for the hard-wall case. These data represented measurements of p_h and p_s as given in equations (A3) and (A7), respectively. If we divide p_s by p_h, we get

$$\frac{p_s}{p_h} = Me^{i\phi} = \frac{1 + \dfrac{e^{ik_s 2\delta_s}}{1 + \dfrac{2\delta_s}{R_{1s}}} \left(\dfrac{1 - \beta}{1 + \beta} + Cs \right)}{\dfrac{R_{1s}}{R_{1h}} e^{i(k_h R_{1h} - k_s R_{1s})} \left(1 + \dfrac{e^{ik_h 2\delta_h}}{1 + \dfrac{2\delta_h}{R_{1h}}} \right)}$$

(B1)

Thus, the data representing the soft-wall measurement were divided by the data from the appropriate hard-wall measurement to determine M and ϕ as a function of frequency.

Equation (B1) cannot be used to calculate β directly because Cs is a nonlinear function of β. A first estimate for β is determined by letting $Cs = 0$. If the form of equation (B1) is taken as

$$Me^{i\phi} = \frac{1 + N\left(\dfrac{1 - \beta_e}{1 + \beta_e} \right)}{D}$$

(B2)

where D is the denominator term of equation (B1)

$$D = \frac{R_{1s}}{R_{1h}} e^{i(k_h R_{1h} - k_s R_{1s})} \left(1 + \frac{e^{ik_h 2\delta_h}}{1 + \dfrac{2\delta_h}{R_{1h}}} \right)$$

(B3)

and N is

$$N = \frac{e^{ik_s 2\delta_s}}{1 + \dfrac{2\delta_s}{R_{1s}}}$$

(B4)

then the estimate for β can be directly calculated.

$$\beta_e = \frac{1 - R}{1 + R}$$

(B5)

where

$$R = Me^{i\phi}\left(\frac{D}{N} \right) - \frac{1}{N}$$

The value of β was determined by using the secant method to solve for the root of the equation

$$\frac{1 - \beta}{1 + \beta} + Cs - R = 0$$

(B6)

where β_e is the starting guess for β. By using the two terms for Cs shown in equation (A6), a value of β was found for each frequency that satisfied equation (B6). The final calculations for impedance and absorption coefficient are

$$\left. \begin{aligned} \frac{Z}{\rho_0 c_0} &= \frac{1}{\beta} \\ \alpha &= 1 - \left| \frac{1 - \beta}{1 + \beta} \right|^2 \end{aligned} \right\}$$

(B7)

In calculations using equations (B1) to (B7), the time dependence was assumed to be $\exp(-i\omega t)$. The measurement impedance was then defined in terms of its real and imaginary parts as $Z = \mathfrak{Re}\{Z\} - i(\mathfrak{Im}\{Z\})$ in order to be consistent with the analytically predicted impedance described in appendix C.

Preliminary data analysis using this approach showed inconsistencies in the results. Measurements of the same treatment location on different days were not repeatable; measurements of treatment locations that should have had similar characteristics gave different impedance and absorption results. Typically, these results were most easily characterized by large decreases in absorption as the frequency increased. In most cases, the different measurements were associated with the movement and resetting of the acoustic source and the microphone.

Two error analyses were performed to find the source of these inconsistencies. First, the sensitivities of the impedance and the absorption coefficient were found for small changes in the propagation velocities and the distances. Table II gives the uncertainties assumed for these parameters from the given

TABLE II.—UNCERTAINTIES USED IN EVALUATING
EFFECTS OF ERRORS IN MEASUREMENT MODEL

Parameter	Baseline value	Uncertainty
Speed of sound, m/s:		
Hard wall, c_h	345	± 0.6
Soft wall, c_s	347	± 0.6
Surface-to-microphone distance, cm:		
Hard wall, δ_h	0.48	± 0.08
Soft wall, δ_s	0.48	± 0.08
Model reflection coefficient at angle of incidence θ, cm:		
Hard wall, R_{1h}	170	± 0.5
Soft wall, R_{1s}	170	± 0.5

baseline values. The impedance and the absorption coefficient were calculated from a measurement of the acoustic treatment in the 9- by 15-ft test section by using the baseline values for the parameters shown in table II. The calculations were then repeated with changes in one parameter at a time. The amount of a change in a parameter was equal to the uncertainty value added to or subtracted from the baseline value. Each time a parameter was changed, the resulting calculations for the impedance and the absorption coefficient were compared with the calculations made by using the baseline values for the parameters. The results of these calculations may be summarized as follows:

(1) Results were insensitive to small changes in either of the propagation velocities.

(2) For a 17-percent change in δ_s, the impedance showed changes on the order of 10 percent from baseline at frequencies greater than 2000 Hz. No changes in the absorption coefficient were apparent. This follows from an examination of equations (B2), (B4), and (B7), where for small δ_s

$$\alpha \approx 1 - |\, Me^{i\phi}D - 1\,|^2$$

which is independent of δ_s because only N is a function of δ_s.

(3) For a 17-percent change in δ_h, the impedance showed changes on the order of 20 percent from baseline at frequencies greater than 1500 Hz, and the absorption coefficient changed by about 10 percent.

(4) It was noted that calculations with small changes in R_{1h} and R_{1s} interacted in such a way that a calculation using R_{1h} plus a small change had the same results as a calculation using R_{1s} minus a small change. Thus, the effects of any changes in R_{1h} and R_{1s} were incorporated into one parameter defined as $(k_h R_{1h} - k_s R_{1s})$. This parameter represents the difference in the times it takes a signal to travel the distance R_{1h} and the distance R_{1s}. For small changes in this parameter, large changes (greater than 100 percent at some frequencies) occurred across the frequency range.

These results indicated that the calculations were sensitive to the distance measurements and that this sensitivity increased with frequency. The measurements of physical distance were

made as accurately as possible; however, the exact location of the center of acoustic radiation within the source remained uncertain, rendering the source-to-microphone distance somewhat inaccurate. A knowledge of the acoustic center location is implicit in deriving equation (B1).

A second error analysis was conducted to determine how the data were affected by the distance changes. By using equation (B1) with an analytical prediction for β (see the section "Model 2" in appendix C), the calculations were performed to determine M and ϕ for the various distance changes. The distance changes affected both M and ϕ, but it is more instructive to consider only ϕ changes because changes in distance or propagation time appear as linear phase shifts in the frequency domain. These are summarized in figure 13. The pattern of changes set forth in the first error analysis is realized in ϕ as changes in slope. Figure 13(a) shows the changes in slope that occur with changes in δ_s. The amount
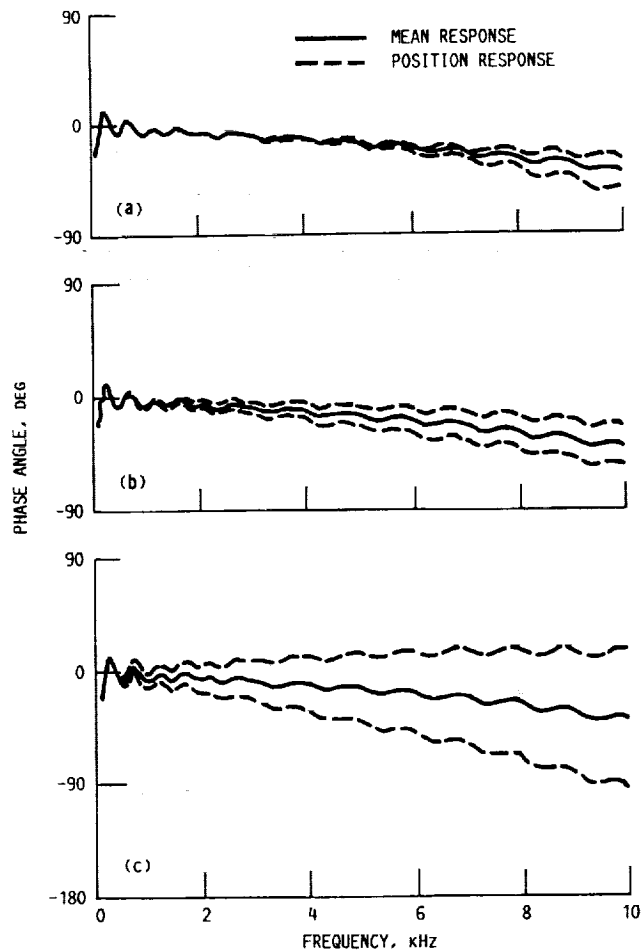
(a) Soft-wall microphone location varied from baseline value (table II) by ± 0.16 cm.

(b) Hard-wall microphone location varied from baseline value (table II) by ± 0.16 cm.

(c) Source location varied from baseline value (table II) by ± 0.5 cm.

Figure 13.—Changes in slope of measurement phase ϕ due to changes in setup geometry.

of change in δ_s is twice as large as the value shown in table II in order to more clearly show changes in the phase plot. With the same changes in δ_h, figure 13(b) shows a slightly larger change in slope. The largest effects on the slope of the phase plot (fig. 13(c)) are again due to small changes in the parameter $k_h R_{1h} - k_s R_{1s}$.

If the same propagation velocity is assumed for both the hard-wall and soft-wall measurements, the changes shown in figure 13(c) are due to a variation of ± 0.5 cm for the difference in the source distance between the two measurements. This 0.3-percent change in the source-to-microphone distance led to the largest errors in making the measurements. It also points to the problem with using TDS. Included in a TDS measurement is the time response of the system, represented by figure 10(d) after proper demodulation of the sweeping signal. The time data are used to set the position of the tracking filter in order to obtain the desired frequency response. A time resolution was inherent in the measurement that for the measurements performed here was $\pm 62.5 \mu s$ or, in terms of distance, approximately ± 2.13 cm. This is four times larger than the distance variation for the slope changes shown in figure 13(c). Thus, the source distance error was within the resolution of the measurement and could not be correctly accounted for during the measurement.

By observing the effects shown in figure 13, a procedure for adding a correction to the data was devised before the calculations for determining β were completed. By expressing equation (B1) as

$$Me^{i\phi} = \frac{1 + M_1 e^{i\theta_1}}{M_2 e^{i\theta_2}\left(1 + M_3 e^{i\theta_3}\right)} \qquad (B8)$$

the phase factor ϕ is found to be

$$\phi \approx \alpha_1 - 2\pi f\left(\frac{R_{1h}}{c_h} - \frac{R_{1s}}{C_s}\right) - 2\pi f \frac{\delta_h}{c_h} \qquad (B9)$$

where

$$\alpha_1 = \tan^{-1}\left(\frac{M_1 \sin \theta_1}{1 + M_1 \cos \theta_1}\right)$$

In deriving equation (B9), the fact that $R_{1h} >> 2\delta_h$ was used to reduce the phase of $1 + M_3 \exp(i\theta_3)$ to simply $\theta_3/2$. If we take the derivative with respect to f, we get

$$\frac{d\phi}{df} \approx \frac{d\alpha_1}{df} - 2\pi\left(\frac{R_{1h}}{c_h} - \frac{R_{1s}}{c_s}\right) - 2\pi \frac{\delta_h}{c_h} \qquad (B10)$$

The right two terms represent constant slopes on a ϕ-versus-f plot. If ϕ is linearized as $\phi = b_1 f + b_2$, then $d\phi/df = b_1$ can be found from a linear least-squares fit of the data ϕ.

In equation (B9), α_1 is a function of δ_s and β. Figure 14 shows a phasor diagram for the determination of α_1. For highly absorbent materials, M_1 is typically small compared with 1. The phase of M_1, $\theta_1 = \Phi + 2k_s\delta_s$, rotates the small vector at the tip of the unit vector as the frequency is varied. Thus, α_1 never gets large. If we assume that there are enough positive and negative phase values, the linearized slope of α_1 versus frequency is near zero. With that assumption, the linearized equation for the slope of the phase becomes

$$b_1 = -2\pi\left(\frac{R_{1h}}{c_h} - \frac{R_{1s}}{c_s}\right) - 2\pi \frac{\delta_h}{c_h} \qquad (B11)$$

Within the time resolution of the TDS measurement, $(R_{1h}/c_h) - (R_{1s}/c_s) = 0$. However, as stated earlier, the two distances may not be exactly the same. Therefore, we replace the factor by an error factor ϵ, which may be considered as an unknown time delay in the system due to an uncertainty in knowing the exact starting point of acoustic radiation and any electromechanical delay in the driver. The error factor ϵ is to be calculated from the data. The error factor as presented here could also include any error in measuring δ_h. By solving for ϵ, we get

$$\epsilon = -\frac{b_1}{2\pi} - \frac{\delta_h}{c_h} \qquad (B12)$$

The correction factor was applied to equation (B5) in order to calculate a corrected estimate for β.

$$\beta_{ec} = \frac{1 - R_c}{1 + R_c}, \qquad R_c = Me^{i\phi}e^{i2\pi f\epsilon}\left(\frac{D}{N}\right) - \frac{1}{N} \qquad (B13)$$

The solution for the root of equation (B6) was repeated with β_{ec} as the starting guess and the replacement of R with R_c. The impedance and the absorption coefficient were again calculated by using equation (B7). An example of the effects of the correction is shown in figure 15. This figure shows the results of two separate measurements of the full-depth treatment taken on different days at different locations on the
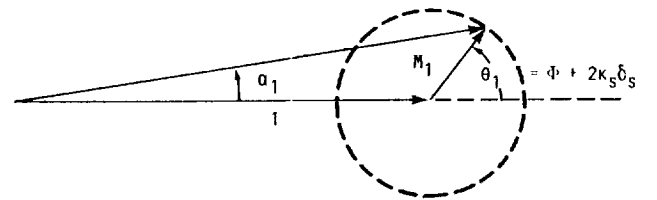

Figure 14.—Diagram representing phase of numerator in equation (B8).

POSITION A
POSITION B

POSITION A, CORRECTED BY 2.69 μs
POSITION B, CORRECTED BY 14.12 μs

(a) Before correction was applied.
(b) After correction was applied.

Figure 15.—Impedance and absorption coefficient comparison of two similar full-depth treatment locations.

test section ceiling. Figure 15(a) shows the uncorrected results; note the differences in both the impedance and the absorption coefficient. After correction, figure 15(b) shows the two measurements to be in close agreement. All the data were corrected in this manner.

Appendix C
Analytical Treatment Models

An analytical model for predicting the input-specific acoustic impedance and the absorption coefficient of the full-depth, two-layer, bulk-absorber treatment was developed with the diagram shown in figure 16 and with the assumption that the incident sound consisted of plane waves. The basic theory for layered treatment may be found in reference 9, and only the final equations for impedance are shown here. With a hard-wall backing, the specific acoustic impedance at the layer 1 side of the perforated plate that covers layer 2 is

$$\frac{Z_2}{\rho_0 c_0} = \frac{W_2}{\rho_0 c_0} \coth(k_2 L_2) + \frac{Z_p}{\rho_0 c_0} \qquad (C1)$$

With equation (C1) as the termination impedance for layer 1, the input-specific acoustic impedance at the outer face of the perforate that covers layer 1 was then determined in the same manner as was equation (C1).

$$\frac{Z_1}{\rho_0 c_0} = \frac{W_1}{\rho_0 c_0} \left[\frac{Z_2 \coth(k_1 L_1) + W_1}{W_1 \coth(k_1 L_1) + Z_2} \right] + \frac{Z_p}{\rho_0 c_0} \qquad (C2)$$

This equation considers the effects of the 20-mesh screen to be negligible at frequencies below 10 kHz. For higher frequencies, an impedance for the screen would have to be added to equation (C2) (see ref. 10).
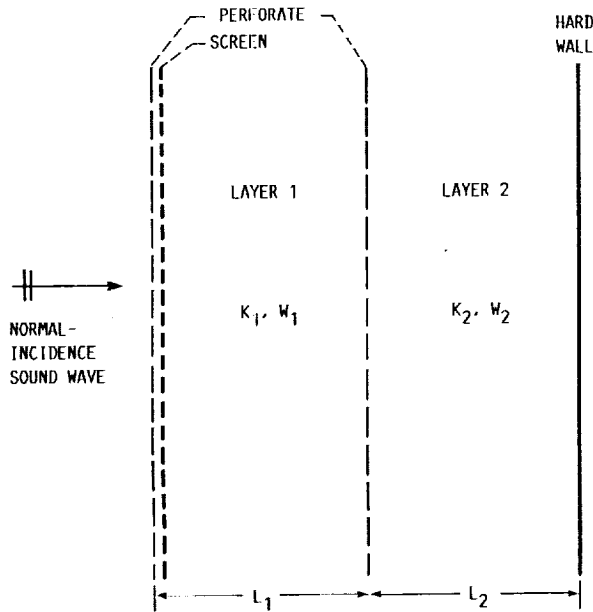

Figure 16.—Diagram of two-layer acoustic treatment with sound wave at normal incidence.

Additional calculations using the impedance were made for the reflection coefficient R_n, the absorption coefficient α, and the specific admittance β.

$$R_n = |R_n| e^{i\psi} = \frac{\dfrac{Z_1}{\rho_0 c_0} - 1}{\dfrac{Z_1}{\rho_0 c_0} + 1} \qquad (C3)$$

$$\alpha = 1 - |R_n|^2 \qquad (C4)$$

$$\beta = \frac{\rho_0 c_0}{Z_1} \qquad (C5)$$

The calculations in this appendix assume the time dependence to be $\exp(i\omega t)$, and the impedance is given in terms of its real and imaginary parts as $Z = \mathfrak{Re}\,[Z] + i(\mathfrak{Im}\,[Z])$.

Perforated-Plate Impedance

The impedance of the perforated plate is based only on viscous and mass effects. The formulation given here was taken from reference 11, equation (7).

$$\frac{Z_p}{\rho_0 c_0} = \frac{\sqrt{8\nu\omega}(t_p + d_p)}{\sigma_p c_0 d_p}(1 + i) + i\,\frac{\omega t_p}{\sigma_p c_0} \qquad (C6)$$

Bulk-Absorber Material Models

A model for the acoustic behavior of the bulk-absorber material is needed to obtain the k and W terms in equations (C1) and (C2). The linearized, one-dimensional equations for continuity, momentum, and state are given in the following form for a differential volume of the material (ref. 12, eqs. (28), (29), and (25)), where $\omega d^2/\nu < 1$:

$$\frac{\partial \rho}{\partial t} = -\rho_0 \frac{1}{H}\frac{\partial u}{\partial x} \qquad (C7)$$

$$\rho_0 \frac{1}{H}\frac{\partial u}{\partial t} = -\frac{\partial p}{\partial x} - \sigma\frac{u}{H} \qquad (C8)$$

$$p = c_e^2 \rho \qquad (C9)$$

By combining equations (C7) to (C9) and assuming that all acoustic quantities are proportional to $\exp(i\omega t - kx)$, we can get the wave equation and subsequently the propagation constant.

$$k^2 = i\left(\frac{\omega}{c_e}\right)^2 \left(\frac{\sigma}{\rho_0 \omega} + i\right) \tag{C10}$$

The characteristic impedance for the material is defined as the ratio of the pressure wave traveling in one direction to the volume velocity in the same direction, $W = p/u$. From equations (C8) and (C10), the normalized characteristic impedance of the porous material is found to be

$$\frac{W}{\rho_0 c_0} = \frac{c_0}{\omega}\left(\frac{c_e}{c_0}\right)^2 \frac{k}{iH} \tag{C11}$$

where in the preceding equations

$$H = 1 - \frac{\rho_b}{\rho_f} \tag{C12}$$

is the porosity of the material. Two models are presented that give equations for calculating σ and c_e.

Model 1.—Hersh and Walker (ref. 12) developed a model to describe the acoustic behavior of a rigid, fibrous, bulk material. This model is based on the empirical relations derived from work done on pressure drop and energy transfer across bundles of circular cylinders or fibers in order to account for viscous loss and heat transfer between the air and the fibers. The model attempts to describe the general behavior of a fibrous material by including terms for both parallel and normal fibers.

The viscous loss term σ is based on a static, one-dimensional pressure drop per unit distance across a bundle of fibers.

$$\frac{\Delta p}{\Delta x} = -\sigma \frac{\mu}{H} \tag{C13}$$

The derivation for σ yields (ref. 12, eq. (13))

$$\sigma = \left(\frac{4\mu}{d^2}\right)(1 - H)(f_n + f_p) \tag{C14}$$

where d is the fiber diameter and the functions f_n and f_p are defined from correlations of static pressure drop data across a bundle of fibers and along parallel bundles of fibers, respectively. In nondimensional form, equation (C14) becomes

$$\frac{\sigma}{\rho_0 \omega} = 4\left(\frac{\nu}{\omega d^2}\right)(1 - H)(f_p + f_n) \tag{C15}$$

where

$$f_p = 3.94(1 - H)^{0.413}[1 + 27(1 - H)^3] \tag{C16}$$

$$F_n = 0.44\,\{16(1 - H)^{0.5}[1 + 14.75(1 - H)^3]\} \tag{C17}$$

The term c_e is called the effective propagation velocity through the porous material. It takes into account the effects of heat transfer between the air and the material. The derivation by Hersh and Walker results in an equation of the form of equation (C9) (ref 12., eq. (25)) where

$$c_e^2 = \frac{c_0^2}{\gamma}\left(\frac{\dfrac{K}{\rho_0 \omega} + i_\gamma}{\dfrac{K}{\rho_0 \omega} + i}\right) \tag{C18}$$

and

$$\frac{K}{\rho_0 \omega} = \frac{4}{Pr}\left(\frac{\nu}{\omega d^2}\right)\left(\frac{1 - H}{H}\right)Nu \tag{C19}$$

and where Pr is the Prandtl number for air and Nu is a Nusselt number correlation for heat transfer between the air and the bundle of fibers.

$$Nu = 5.4(1 - H)^{0.5}[1 + 3.94(1 - H)^3] \tag{C20}$$

Model 2.—Although the rigid-fiber model of Hersh and Walker gives reasonable predictions for sound absorption, its accuracy is limited by the use of a static viscous loss term (eq. (C14)). In material models of the form given by equations (C7) to (C9), the viscous loss term σ is a complex function of frequency representing the physical fact that the viscous forces can be out of phase with the velocity. Lambert and Tesar (ref. 13) used this approach for viscous loss in their wave-decoupling model for fibrous material. The resulting propagation constant through the material can be put into the same form, after some manipulation, as equation (C10). The viscous loss term and the effective propagation velocity become

$$\frac{\sigma}{\rho_0 \omega} = 16K'\left(\frac{\nu}{\omega d^2}\right)\left(\frac{1 - H}{H}\right)^2 F(\kappa) \tag{C21}$$

$$c_e^2 = \frac{c_0^2}{\gamma}\left(\frac{\dfrac{\omega_T}{\omega} + i\gamma}{\dfrac{\omega_T}{\omega} + i}\right) \qquad (C22)$$

where

$$\kappa = \frac{1}{2}\,\frac{H}{1-H}\left(\frac{\omega d^2}{\nu}\right)^{1/2} \qquad (C23)$$

$$F(\kappa) = \frac{\bar{\kappa}^2 J_1(\bar{\kappa})}{8J_1(\bar{\kappa}) - 4\bar{\kappa}J_0(\bar{\kappa})} \qquad \bar{\kappa} = (-i)^{0.5}\kappa \quad (C24)$$

$$\frac{\omega_T}{\omega} = \frac{16K'}{Pr}\left(\frac{\nu}{\omega d^2}\right)\left(\frac{1-H}{H}\right)^2 \qquad (C25)$$

and J_0 and J_1 are cylindrical Bessel functions of zeroth and first order, respectively. The derivation of the complex viscosity correction function $F(\kappa)$, which accounts for the phase relationship between the relative air velocity and the viscous forces, can be found in Biot (ref. 14) or Attenborough (ref. 15).

The constants used in the model calculations are given in table III, and a comparison between models 1 and 2 is shown in figure 17.

TABLE III.—CONSTANTS USED IN TWO-LAYER ACOUSTIC
TREATMENT MODEL TO PREDICT ACOUSTIC
IMPEDANCES AND ABSORPTION
COEFFICIENTS

|	
Adiabatic speed of sound, c_0, m/s	344
Fiber diameter, d	1.254×10^{-5} m
Diameter of holes in perforated plate, d_p, cm	0.32
Kozeny constant, K'	7.26
Depth of layer 1, L_1, cm	17.2
Depth of layer 2, L_2, cm	17.2
Prandtl number for air, Pr	0.71
Thickness of perforated plate, t_p, cm	0.16
Ratio of specific heats for air, γ	1.4
Kinematic viscosity of air, ν	1.51×10^{-5} m²/s
Bulk density of layer 1, ρ_{b1}, kg/m³	6.4
Bulk density of layer 2, ρ_{b2}, kg/m³	17.7
Density of fiber material, ρ_f, kg/m³	1440
Porosity of perforated plate, σ_p	0.4
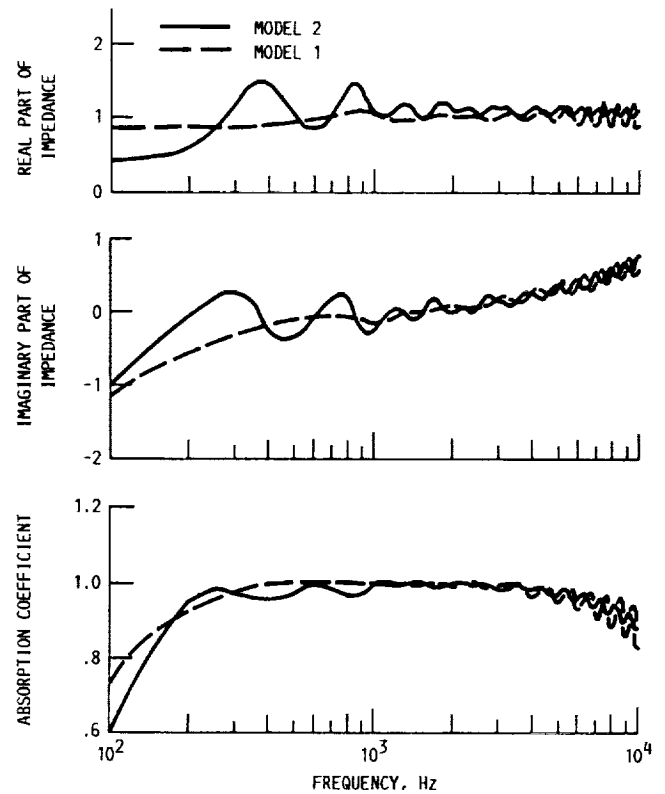
Figure 17.—Impedance and absorption coefficient comparisons between predictions for two-layer treatment using model 1 and model 2.

Appendix D
Angle of Incidence

The specific acoustic impedance and the absorption coefficient were determined for a plane wave at an angle of incidence to the treatment (fig. 18). In this case, the wave was allowed to refract at each boundary existing in the treatment (see, for example, ref. 9). With a hard-wall backing, the specific acoustic impedance at the layer 1 side of the perforated plate covering layer 2 is

$$\frac{Z_2}{\rho_0 c_0} = \frac{W_2}{\rho_0 c_0 K_2} \coth(k_2 L_2 K_2) + \frac{Z_p}{\rho_0 c_0} \tag{D1}$$

By using equation (D1) as the termination impedance for layer 1, the input-specific acoustic impedance at the outer face of the perforate that covers layer 1 is

$$\frac{Z_1}{\rho_0 c_0} = \frac{W_1}{\rho_0 c_0 K_1} \left[\frac{Z_2 K_1 \coth(k_1 L_1 K_1) + W_1}{W_1 \coth(k_1 L_1 K_1) + Z_2 K_1} \right] + \frac{Z_p}{\rho_0 c_0} \tag{D2}$$

where

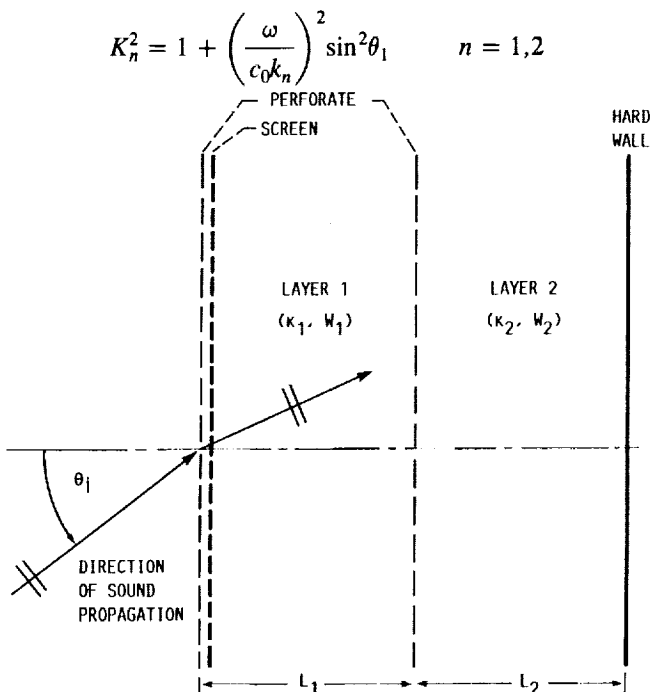$$K_n^2 = 1 + \left(\frac{\omega}{c_0 k_n}\right)^2 \sin^2 \theta_1 \qquad n = 1,2$$

Figure 18.—Diagram of two-layer acoustic treatment with sound wave at angle of incidence.

Additional calculations using the impedance were made for the reflection coefficient R_i and the absorption coefficient α_i.

$$R_i = \frac{\dfrac{Z_1}{\rho_0 c_0} \cos \theta_i - 1}{\dfrac{Z_1}{\rho_0 c_0} \cos \theta_i + 1} \tag{D3}$$

$$\alpha_i = 1 - |R_1|^2 \tag{D4}$$

The results of using material model 2 in the calculations of the impedance and the absorption coefficient are shown in figure 19 for incidence angles of 15°, 30°, and 45°. In the 9- by 15-ft test section, the maximum angle of incidence to the treatment for a typical source-microphone arrangement was about 45°. Therefore, these angles are representative of that
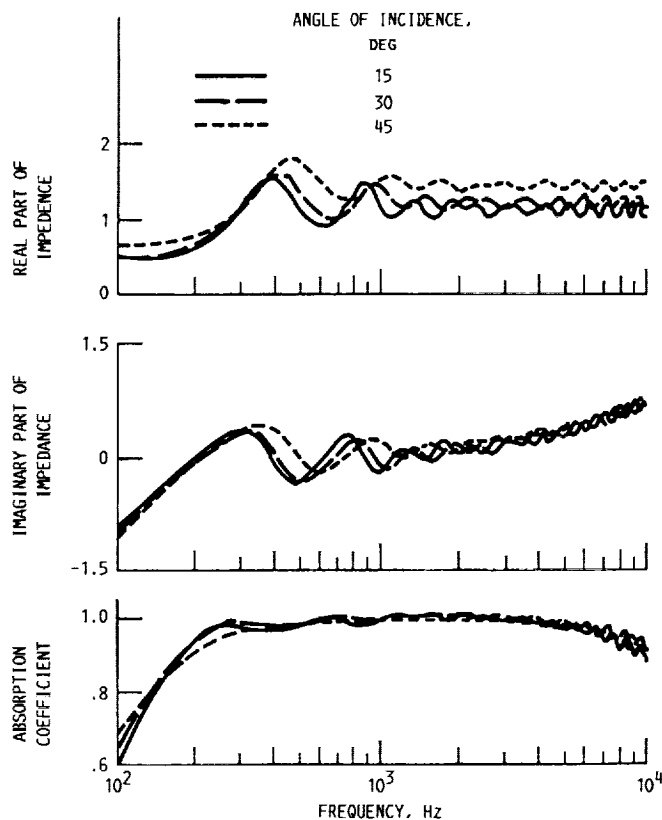
Figure 19.—Impedance and absorption coefficient calculations for angle-of-incidence effects on 9- by 15-ft test section treatment using model 2 in predictions.

22

incidence range. The oscillation in the impedance shifted toward higher frequencies as the angle increased, and the real part of the impedance generally increased at most frequencies. The resulting absorption coefficient did not change significantly over this 45° incidence range. These calculations show that, even though no angle-of-incidence measurements were properly made for the treatment in the 9- by 15-ft test section, the normal-incidence measurements are good indicators of the treatment's impedance and absorption characteristics out to a 45° angle of incidence.

Appendix E
Symbols

A	acoustic source characteristics parameter		S	sweep rate
B	measurement tracking filter bandwidth		T	measurement time window
b_1	linearized slope of measured phase ϕ		t	time
Cs	spherical wave correction factor, equation (A6)		t'	group delay time, equation (A8)
c	speed of sound		t_p	thickness of perforated plate
c_e	effective propagation velocity, equations (C18) and (C22)		W	characteristic impedance
			X	treatment thickness
c_0	adiabatic speed of sound		Z	acoustic impedance
D	denominator term of equations (B1) and (B3)		Z_p	perforate acoustic impedance, equation (C6)
d	fiber diameter		α	normal absorption coefficient, equation (C4)
d_p	diameter of holes in perforated plate		α_i	absorption coefficient at angle of incidence θ_i, equation (D4)
Δd_{ij}	path length difference between path i and path j			
Ei	exponential integral, reference 5		α_1	phase of numerator, equations (B8) and (B9)
$F(\kappa)$	viscosity correction function, equation (C24)		β	normal specific acoustic admittance
f	frequency		γ	ratio of specific heats
f_n	pressure drop correlation, normal fibers, equation (C17)		δ	surface-to-microphone distance
			ϵ	correction factor, equation (B12)
f_p	pressure drop correlation, parallel fibers, equation (C16)		θ_i	angle of incidence, figure 17
			θ_m	model phase factors (compare eqs. (B8) and (B1)), m = 1,2,3
Δf	frequency resolution			
Δf_{ij}	frequency shift between signals i and j		κ	dimensionless parameter, equation (C23)
H	porosity, equation (C12)		μ	viscosity
i	$\sqrt{-1}$		ν	kinematic viscosity
J_0	zeroth-order cylindrical Bessel function		ρ_b	bulk density
J_1	first-order cylindrical Bessel function		ρ_f	density of fiber material
K	heat transfer parameter, equation (C18)		ρ_0	ambient air density
K'	Kozeny constant		σ	viscous loss term, equations (C15) and (C21)
k	propagation constant		σ_p	porosity of perforated plate
L	depth of treatment layer		Φ	phase of $(1 - \beta)/(1 + \beta) + Cs$
M	amplitude of measured data, equation (B1)		ϕ	phase of measured data, equation (B1)
M_m	model amplitude factors (compare eqs. (B8) and (B1), m = 1,2,3		ψ	reflection coefficient phase, equation (C3)
			ω	radian frequency
N	numerator factor of equations (B1) and (B4)		ω_T	thermal characteristic frequency, equation (C25)
Nu	Nusselt number correlation, equation (C20)			

Pr	Prandtl number		**Subscripts:**	
p	acoustic pressure		c	corrected term, appendix B
R	reflection coefficient factor, equation (B5)		e	first estimate of term, appendix B
R_i	model reflection coefficient at angle of incidence θ_i, equation (D3)		h	term applies to hard-wall measurements
			s	term applies to soft-wall measurements
R_n	model reflection coefficient at normal incidence, equation (C3)		1	layer 1 of treatment model, appendixes C and D
			2	layer 2 of treatment model, appendixes C and D
R_1	source-to-microphone distance			
R_2	image-source-to-microphone distance, equation (A2)			

References

1. Rentz, P.E.: Softwall Acoustical Characteristics and Measurement Capabilities of the NASA Lewis 9 × 15 Foot Low Speed Wind Tunnel. (BBN-3176, Bolt, Beranek and Newman Inc.; NASA Contract NAS3-19410) NASA CR-135026, 1976.

2. Dahl, M.D.; and Rice, E.J.: Measured Acoustic Properties of Variable and Low Density Bulk Absorbers. NASA TM-87065, 1985.

3. Yuska, J.A.; Diedrich, J.H.; and Clough, N.: Lewis 9- By 15-Foot V/STOL Wind Tunnel. NASA TM X-2305, 1971.

4. Ingard, U.; and Bolt, R.H.: A Free Field Method of Measuring the Absorption Coefficient of Acoustic Materials. J. Acoust. Soc. Am., vol. 23, no. 5, Sept. 1951, pp. 509–516.

5. Nobile, M.A.; and Hayek, S.I.: Acoustic Propagation Over an Impedance Plane. J. Acoust. Soc. Am., vol. 78, no. 4, Oct. 1985, pp. 1325–1336.

6. Morse, P.M.; and Ingard, K.U.: Theoretical Acoustics. McGraw-Hill, 1968.

7. Heyser, R.C.: Acoustical Measurements by Time Delay Spectrometry. J. Audio Eng. Soc., vol. 15, no. 4, Oct. 1967, pp. 370–382.

8. Skudrzyk, E.J.: The Foundations of Acoustics. Springer-Verlag, 1971, p. 309.

9. Brekhovskikh, L.M.: Waves in Layered Media. Academic Press, 1960.

10. Rice, E.J.: A Model for the Acoustic Impedance of Linear Suppressor Materials Bonded on Perforated Plate. AIAA Paper 81-1999, Oct. 1981 (NASA TM-82716).

11. Guess, A.W.: Calculation of Perforated Plate Liner Parameters from Specified Acoustic Resistance and Reactance. J. Sound Vibr., vol. 40, no. 1, May 8, 1975, pp. 119–137.

12. Hersh, A.S.; and Walker, B.: Acoustic Behavior of Fibrous Bulk Materials. AIAA Paper 80-0986, June 1980.

13. Lambert, R.F.; and Tesar, J.S.: Acoustic Structure and Propagation in Highly Porous, Layered, Fibrous Materials. J. Acoust. Soc. Am., vol. 76, no. 4, Oct. 1984, pp. 1231–1237.

14. Biot, M.A.: Theory of Propagation of Elastic Waves in a Fluid-Saturated Porous Solid, II. Higher Frequency Range. J. Acoust. Soc. Am., vol. 28, no. 2, Mar. 1956, pp. 179–191.

15. Attenborough, K.: Acoustical Characteristics of Porous Materials. Phys. Rept., vol. 82, no. 3, Feb. 1982, pp. 179–227.

NASA
National Aeronautics and
Space Administration

Report Documentation Page

1. Report No. NASA TP-2996	2. Government Accession No.	3. Recipient's Catalog No.

4. Title and Subtitle		5. Report Date
Comparison Between Design and Installed Acoustic Characteristics of NASA Lewis 9- by 15-Foot Low-Speed Wind Tunnel Acoustic Treatment		April 1990
		6. Performing Organization Code

7. Author(s)	8. Performing Organization Report No.
Milo D. Dahl and Richard P. Woodward	E-4981
	10. Work Unit No. 505-62-21

9. Performing Organization Name and Address	11. Contract or Grant No.
National Aeronautics and Space Administration Lewis Research Center Cleveland, Ohio 44135-3191	
	13. Type of Report and Period Covered Technical Paper

12. Sponsoring Agency Name and Address	
National Aeronautics and Space Administration Washington, D.C. 20546-0001	14. Sponsoring Agency Code

15. Supplementary Notes

16. Abstract

The test section of the NASA Lewis 9- by 15-Foot Low-Speed Wind Tunnel was acoustically treated to allow the measurement of sound under simulated free-field conditions. The treatment was designed for high sound absorption at frequencies above 250 Hz and for withstanding the environmental conditions in the test section. In order to achieve the design requirements, a fibrous, bulk-absorber material was packed into removable panel sections. Each section was divided into two equal-depth layers packed with material to different bulk densities. The lower density was next to the facing of the treatment. The facing consisted of a perforated plate and screening material layered together. Sample tests for normal-incidence acoustic absorption were also conducted in an impedance tube to provide data to aid in the treatment design. Tests with no airflow, involving the measurement of the absorptive properties of the treatment installed in the 9- by 15-foot wind tunnel test section, combined the use of time-delay spectrometry with a previously established free-field measurement method. This new application of time-delay spectrometry enabled these free-field measurements to be made in nonanechoic conditions. The results showed that the installed acoustic treatment had absorption coefficients greater than 0.95 over the frequency range 250 Hz to 4 kHz. The measurements in the wind tunnel were in good agreement with both the analytical prediction and the impedance tube test data.

17. Key Words (Suggested by Author(s))	18. Distribution Statement
Acoustic treatment; Acoustic treatment design; Acoustic treatment measurement; Bulk absorbers; Wind tunnel acoustic treatment	Unclassified – Unlimited Subject Category 09

19. Security Classif. (of this report)	20. Security Classif. (of this page)	21. No of pages	22. Price*
Unclassified	Unclassified	29	A03